2022

Synchronous Raman Microspectroscopy and Laser Beam Induced Current Measurements as a Metrology Tool for Solar Cells and Optoelectronic Devices

Jeya Prakash Ganesan
University of Central Florida

SYNCHRONOUS RAMAN MICROSPECTROSCOPY AND LASER BEAM INDUCED CURRENT MEASUREMENTS AS A METROLOGY TOOL FOR SOLAR CELLS AND OPTOELECTRONIC DEVICES

by

JEYA PRAKASH GANESAN
Master of Science, University of Central Florida, USA, 2018
Bachelor of Engineering, Anna University, India, 2015

A dissertation submitted in partial fulfillment of the requirements
for the degree of Doctor of Philosophy
in the Department of Materials Science and Engineering
in the College of Engineering and Computer Science
at the University of Central Florida
Orlando, Florida

Spring Term
2022

Major Professor: Parag Banerjee

ABSTRACT

This works developed synchronous Raman microspectroscopy with laser beam induced current (LBIC) measurements to generate insights into structure-property correlations in finished solar cell modules. Raman spectroscopy is a powerful, non-destructive technique to examine phase and composition of materials where a laser beam excites characteristic vibrational modes of chemical bonds in a material. Conducting Raman spectroscopy under a microscope (i.e., Raman microspectroscopy) with confocal capabilities allows the chemical constituents to be mapped with high spatial resolution in the *x, y* and *z* directions. Simultaneously, the excitation laser from Raman can also generate photocarriers in a semiconductor. In a solar cell, these photocarriers generate a current termed as, LBIC which measures the device's ability to produce current upon light illumination. Thus, mapping the chemical signatures *and* electrical characteristics synchronously across the *x, y* and *z* directions can provide a deeper understanding and a multi-modal metrology platform for solar cell materials and devices. Simultaneous Raman microspectroscopy and LBIC measurement technique can be used to identify differences in quality between fresh and degraded solar cells through Raman microspectroscopy. The technique can be used to study material device correlation in solar cells with LBIC coupling. Coupled with LBIC, these measurements will provide deeper insights to cell quality and reliability. The proposed system is material agnostic and can be applied to a generalized photonic device. Effective *in-line* metrology in solar cell manufacturing holds the potential for reducing $/watt of solar cells by identifying process and materials excursions sufficiently early in the production process, thus improving manufacturing efficiency and reducing material loss. Effective metrology requires a characterization technique

with adequate sensitivity, scale, and spatial resolution. While optical and electrical techniques are routinely used for *in-line* metrology and inspection, they do not generate the desired scientific understanding that correlate processes with materials and device performance. Thus, by applying the technique of combined Raman and LBIC measurements, understanding the interplay between process-material-device characteristics of a solar cell can be elucidated. Such knowledge is expected to positively impact the solar cell manufacturing industry.

To *Appa*, *Amma* and *Arun*

ACKNOWLEDGEMENTS

I wish to thank my advisor, Dr. Parag Banerjee, for offering the support and guidance throughout the course of my study and research at UCF. I would also like to thank all my committee members, Dr. Laurene Tetard. Dr. Kristopher O. Davis, Dr. Tania Roy and Dr. Titel Jurca for providing their valuable time for this dissertation and discussion.

I am thankful to my colleagues, Corbin Feit, Jaynlynn Sosa, Novia Berriel, Brian Butkus, Nafis Iqbal, Jannatul Mousumi, Durjoy Dev, Adithi Krishnaprasad, Molla Islam and Ricardo Martinez for their support and encouragement from practice presentations to experimental discussions.

I am thankful to Nanoscience Technology Center, Materials Characterization Facility for offering all the facilities required for conducting my research.

I am thankful to several organizations such as IEEE, The Electrochemical Society, American Vacuum Science for giving me the opportunity to present my research to the scientific community during their annual technical meetings.

I acknowledge the support from the Funding agency – National Science Foundation (Award No. 1922984), National Science Foundation Major Research Instrumentation (Award No. 1920050 for confocal Raman and 1726636 for measuring XPS).

Most of all, I am thankful to my parents and brother for their undivided support throughout my work.

TABLE OF CONTENTS

LIST OF FIGURES

LIST OF TABLES

LIST OF ACRONYMS (or) ABBREVIATIONS

ARC	Antireflective Coating
CCD	Charged-coupled Device
CdTe	Cadmium Telluride
CIGS	Copper Indium Gallium Diselenide
c-Si	Crystalline Silicon
EBIC	Electron Beam Induced Current
EDX	Energy Dispersive X-ray Spectroscopy
EL	Electroluminescence
GB	Grain Boundary
IEC	International Electrochemical Commission
IQE	Internal Quantum Efficiency
LBIC	Laser Beam Induced Current
mc-Si	Multicrystalline Silicon
MEMS	Micro-electromechanical Systems
nc-Si	Nanocrystalline Silicon
PECVD	Plasma Enhanced Chemical Vapor Deposition
PL	Photoluminescence
PV	Photovoltaics
SEM	Scanning Electron Microscopy
Si	Silicon
SiH_4	Silane
TO	Transverse Optical

XRD X-ray Diffraction

CHAPTER ONE: INTRODUCTION

Technological advances in solar cell manufacturing at economies-of-scale have led to a significant decrease in the price of solar cells. Additionally, new materials and improved processes have steadily led to the increase of solar cell efficiencies (currently at 26.7 % for silicon (Si) solar cells) and reliability (20 years with < 5.6 % degradation in open circuit voltage (V_{oc})) [1-3]. Consequently, costs for energy generation using Si solar cells have dropped to 0.038 $/kW-hr, which puts it at par with other sources of non-renewables such as, coal (0.12 $/kW-hr) and hydroelectric (0.039 $/kW-hr) [4]. Si solar cells capture a significant portion (90 %) of the solar cell market [5]. The high-volume manufacturing environments for Si solar cells integrate processes that dope precise regions in the absorber layers, create textured surfaces that efficiently absorb solar irradiation, integrate transparent conductors and metallic films onto the device, while packaging, wiring and laminating cells into modules [6]. Today, the Si solar cell is a complex stack of materials with specific electrical, optical, structural, and mechanical functionalities.

For continued cost and efficiency gains in Si solar cell manufacturing, in-line metrology and characterization tools play a critical role. With the right modality of measurement and a well-designed tool, process excursions, material variations and their impact on device performance can be detected sufficiently early to avoid losses in productivity. Techniques such as, optical inspection and electrical testing are present in manufacturing lines. However, these techniques measure performance at the module level and either lack the sensitivity or spatial resolution to map deviations from process excursions on a solar cell. To the best of our knowledge, advanced materials characterization techniques with high sensitivity at the micron scale have not been implemented [7].

There are many metrology methods used in each step of the industrial production of PVs along the supply chain process. Raman microspectroscopy is used in detecting crack formation in all the PV production processes. LBIC is used in detecting poor junction isolation and many other processes [8-10].

The central hypothesis of this proposal is that the laser source used for performing Raman microspectroscopy to analyze structure property relationship of the target material can also be used to perform LBIC measurements for any photonic device.

Thus, by coupling a Raman + LBIC system together, the correlation of structure of materials in a solar cell to device performance can be studied.

From a research perspective, we note that Raman microspectroscopy has been used to characterize CdS/CdTe based solar cells [11]. However, Raman microspectroscopy is currently *not* optimized for Si solar cell characterization. The measurements are slow and usually take several minutes to be acquired. With proper hardware modifications including use of multiple heads, faster raster scans and optimized signal acquisition algorithms, it is possible to acquire data in time scales which are well within the requirements of high-volume solar cell manufacturing environments.

LBIC is one of the most accurate tools to determine defects in solar cells. LBIC is a complimentary technique to EBIC (Electron Beam Induced Current) which is performed in a SEM (Scanning Electron Microscopy). LBIC uses similar instrumentation to Raman, shining light at various positions of the sample to produce a photo response map. However, the spatial resolution is compromised when using LBIC over EBIC (<1 μm for EBIC, <(10–20) μm for LBIC) [12]. Susanne et al., developed a technique to characterize solar cells using a microscopic light beam

for higher resolution[13]. The microscopic LBIC measurement showed good correlation to EBIC. Thus, the need of sample preparation and vacuum condition is not required using this technique.

Performing synchronous LBIC with Raman microspectroscopy, photo inactive areas can be identified at the micro-scale. This clearly has the advantage of characterizing solar cells in ambient conditions without any sample preparations. Material-device correlation can be established from performing synchronous Raman microspectroscopy and LBIC measurements. Any photonic device with a Raman fingerprint can be studied with the proposed technique.

CHAPTER TWO: MOTIVATION

Defects identification is a vital part of the PV production process. As mentioned earlier, there are many methods used in characterizing solar cells. Electroluminescence (EL) and photoluminescence (PL) are the two most common used methods. PL is the emission of light after photon absorption. When a light is shined on a PV material, the electrons are excited from the ground state to the conductive state. These excited electrons return to the ground state by releasing its energy in the form of light thus producing a PL image or map.

In this section, PL image of both fresh and degraded Si solar cell (samples described later in Chapter Five) is shown to understand this single mode method of characterizing solar cells.

2.1 Methodology

A BT Imaging LIS-R1 PL system was used in this experiment featuring an 808 nm wavelength laser as the excitation source. The test samples were imaged at 1.28 suns (highest illumination power achievable by the tool). The emitted PL signal was captured by a 1-megapixel Si charge-coupled device (CCD) camera with a 920 nm long-pass filter. In this experiment, a photon flux of 3.085×10^{17} cm^{-2} s^{-1} was assumed to be 1 sun. This was determined by using a photon flux that allows a reference cell to match the short-circuit current density (J_{sc}) derived from known external quantum efficiency data.

2.2 Results and Discussion

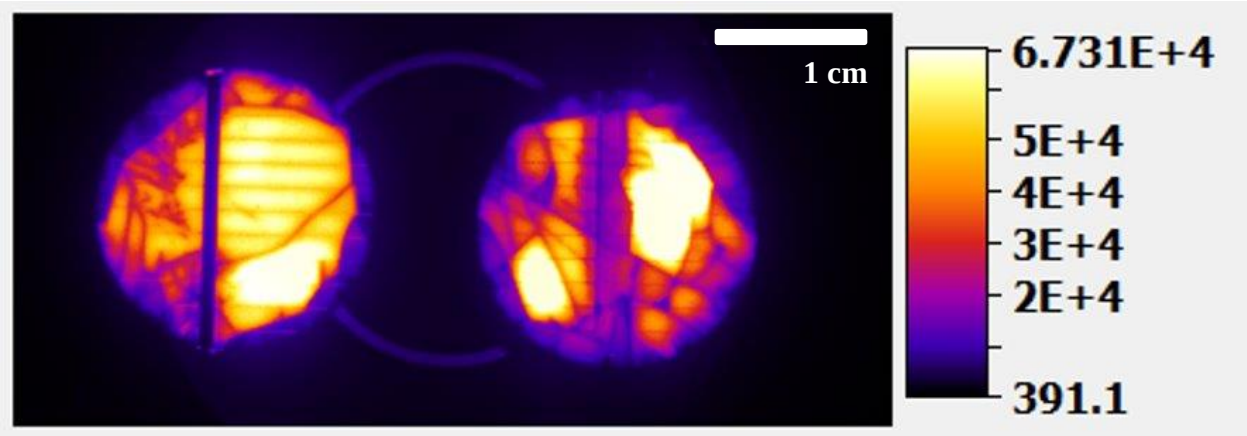

Figure 1: PL image (intensity) of fresh and degraded solar cell. The maximum value (counts) of the PL peak is mapped here with the range shown in the color scale.

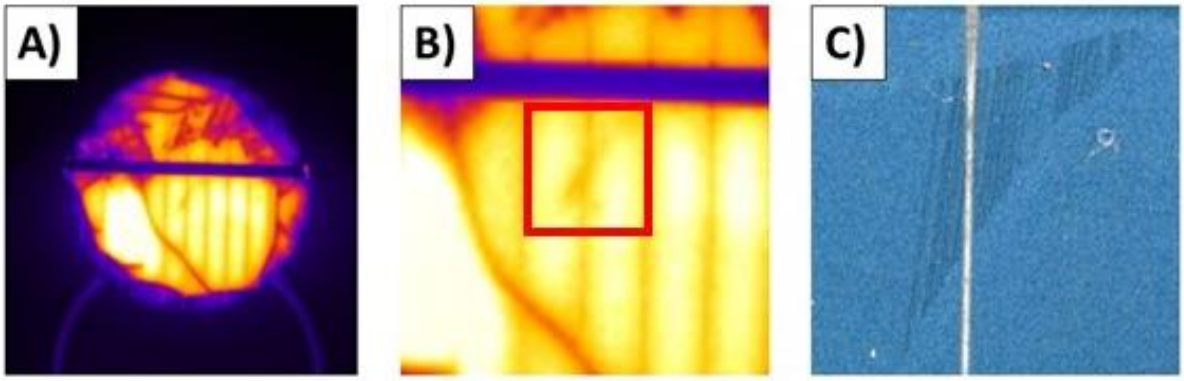

Figure 2: A) PL image of fresh solar cell B) PL image showing a highlighted region with a lower intensity (Size of the micrograph is 10.14 mm × 10.14 mm) C) Optical micrograph of finger 6 showing saw marks (Size of the micrograph is 4.38 mm × 4.38 mm). PL image used has the same color range as Figure 1.

Figure 1 shows the PL image of fresh and degraded Si solar cell. The fresh cell shows higher PL intensity compared to the tested cell as expected. Several cracks were observed on both the cells but were very predominant in the degraded cell. This could be attributed to the damp heat

testing conducted on the cell. **Figure 2A** shows the PL image of fresh Si solar cell. **Figure 2B** shows the zoomed in image of **Figure 2A**. The red boxed region shows a shaded region indicating lower PL intensity. When looked at optical micrographs of the untested Si solar cell, it was confirmed that the shaded region on PL map is matched to the saw mark observed on an Ag finger shown in **Figure 2C**. This shows PL can characterize defects such as saw marks on solar cells in macro scale.

Although, this technique was quick and easy in characterizing defects in solar cells, with the application of combined Raman microspectroscopy and LBIC, spatial resolution will be increased in micron scale. Information on mechanical stress around cracks and defects can be obtained. The quality of solar cells with higher spatial resolution can be studied. This work emphasizes the effectiveness of synchronous Raman and LBIC measurement in characterizing solar cells that correlate materials structure property to device performance.

This work is divided into the following chapters. In chapter 3 background information on solar cells and their production, Raman microspectroscopy and LBIC are briefly described. In chapter 4, the instrumentation to measure synchronous Raman and LBIC measurement is described. In chapter 5, the work on Raman microspectroscopy of a multicrystalline Si solar cell is described. Chapter 6 talks the use of Raman microspectroscopy in characterizing a damp heat tested solar cell. In Chapter 7, the synchronous Raman and LBIC measurement modality is used to characterize a crystalline Si solar cell with focus on laser induced damages, defect and Ag metallization. Chapter 8 talks about conclusion and future perspectives of this work.

CHAPTER THREE: BACKGROUND

3.1 Solar Cells

Solar cells or photovoltaic cells convert sunlight into electricity. The clean renewable energy source has many benefits such as a limitless source of energy (i.e., sun), and a reduction of carbon dioxide emissions. Factors such as materials, device construction (layers) and wiring and busing affect the efficiency of a solar cell. Monocrystalline Si, polycrystalline Si and thin film based solar cells are the main technologies used in the photovoltaics industry. Hybrid organic-inorganic perovskites are the new emerging thin film photovoltaic technology along with organic solar cells, dye-sensitized solar cells, and quantum dots [14, 15].

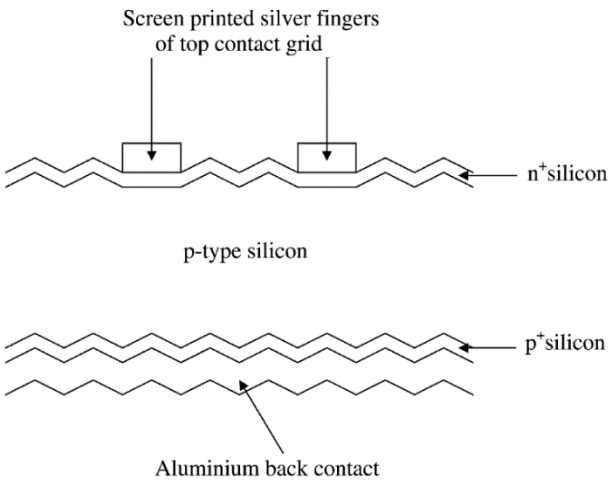

Figure 3: Cross sectional view of a commercial Si solar cell with screen-printed contacts [6].

Solar cells work on the principle of photovoltaic effect, where a potential difference is generated at the junction of two different materials in response to electromagnetic radiation. Semiconductor can be of two types: direct band gap and indirect band gap and is usually used as an absorber. Absorption of a photon in a semiconductor excites an electron from an initial energy level to a higher energy level. This creates a void with a positive elementary charge leading to the

generation of electron-hole pair. To use the energy stored in the electron-hole pair for performing work in an external circuit, carrier selective contacts must be present on both sides of the absorber. These are the *n* and *p*-type materials. The thickness of the absorber plays an important role as the solar cell design and should allow the electron and hole to reach the contacts before recombination. With electrical contacts, the charge carriers are extracted and can perform work in an external circuit [15]. **Figure 3** shows the schematic cross-sectional view of a commercial Si solar cell.

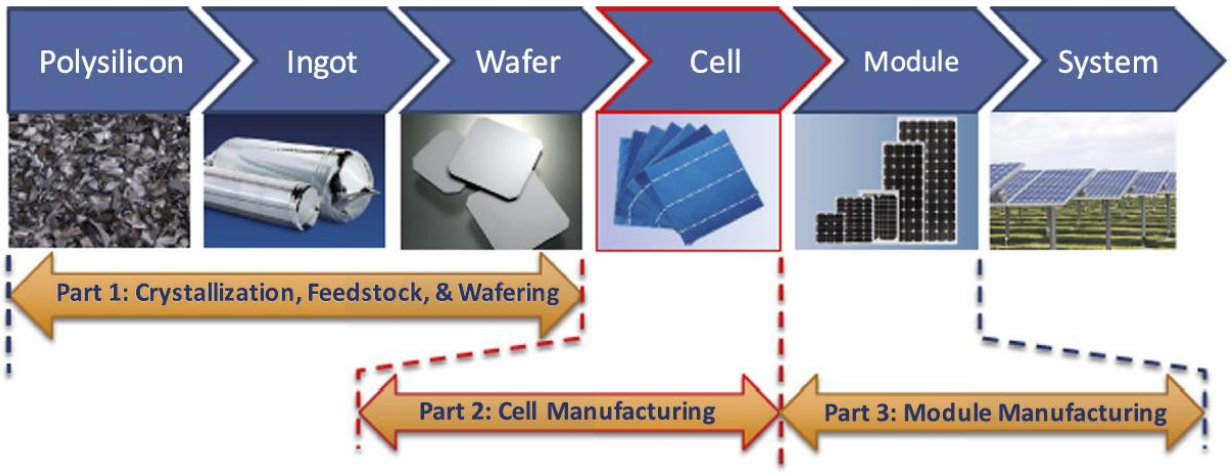

Figure 4: Schematic representation of c-Si PV manufacturing area across the supply chain [8].

Si is the most common semiconductor material used for manufacturing solar cells because of its efficiency [5]. Si wafer is cut from a large crystal grown using Czochralski method, doped with boron acceptor impurities. The wafers are mechanically polished to remove the saw marks and chemically polished. The surface is textured and then a *pn* junction is produced by diffusing phosphorous. Electrical contacts are screen-printed to connect to an external circuit [16]. **Figure 4** shows the production of solar cells from polysilicon.

Second generation solar cells comprises of thin films of amorphous Si usually produced via plasma-enhanced chemical vapor deposition (PECVD) of gases containing silane (SiH_4). The

amorphous Si contains an alloy of Si and hydrogen in which the hydrogen plays the important role of passivating the dangling bonds that result from the random rearrangement of Si atoms. Cadmium telluride (CdTe) and copper gallium indium diselenide (CIGS) are also important absorber materials for thin film solar cells. Organic-inorganic hybrid perovskites solar cells are third generation solar cells that have been developed recently for photovoltaic applications. They have wide variety of advantages such as low cost, ease of production, installation, and low energy payback time with power conversion efficiency over 22% [17-22].

3.2 Raman Microspectroscopy

When light of wavelength 'λ' is incident on matter, there is a finite probability that light will be scattered at the same frequency. This elastic process is called Rayleigh scattering. The resulting 'virtual state' of the molecule is a very short-lived distortion of the electron cloud caused by the oscillating electric field of the incident light. This electron cloud is also influenced by molecular vibrations leading to Raman scattering. The scattered photon is lower (or higher) in energy by an amount equal to a bond vibrational transition leading to Stokes (anti-Stokes) modes in the Raman spectrum. The concept of vibrational transitional modes is shown in **Figure 5**.

Raman scattering depicted in **Figure 6** is a result of the polarization induced in the molecule by the oscillating electric field of the incident light. The induced dipole radiates scattered light, with or without exchanging energy with vibrations in the molecule. The light is scattered at three frequencies assuming that the polarized electrons will radiate light at the frequency of their oscillations. Rayleigh scattering occurs at the same frequency as the laser. It has a magnitude proportional to the inherent polarizability of the molecule. Stokes Raman scattering occurs when

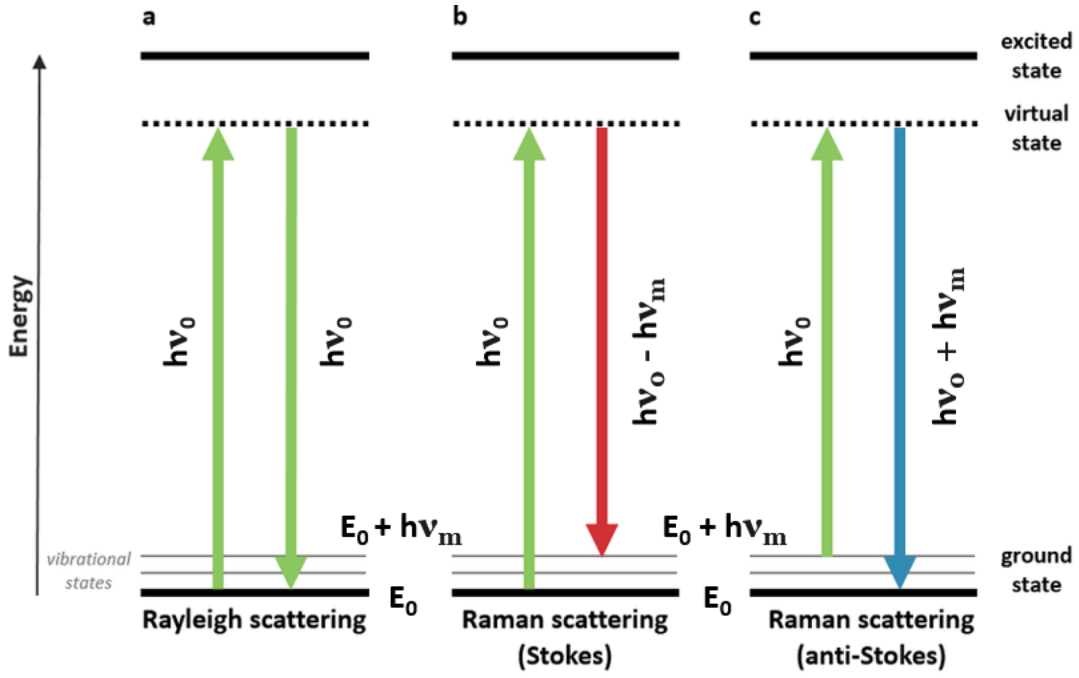

Figure 5: Spectroscopic transitions underlying several types of vibrational spectroscopy [23].

the molecule gains energy from the incident light and the scattered light loses energy which increases the wavelength. Anti-Stokes Raman scattering occurs when the molecule loses energy from the incident light and the scattered light gains energy which decreases the wavelength.

The following insights are useful when it comes to Raman scattering. Polarization and scattering intensities are linear with the laser intensity. Only vibrations that change the polarizability produce Raman scattering. Raman shifts may be both positive and negative. Anti-stokes Raman intensity depends on the population of the first vibrationally excited state and its intensity is related to temperature by the Boltzmann distribution. Polarizability may vary for different molecules and for different modes in a given molecule which leads to wide variations in Raman scattering intensity. Raman scattering is much weaker when compared to Rayleigh scattering [24, 25].

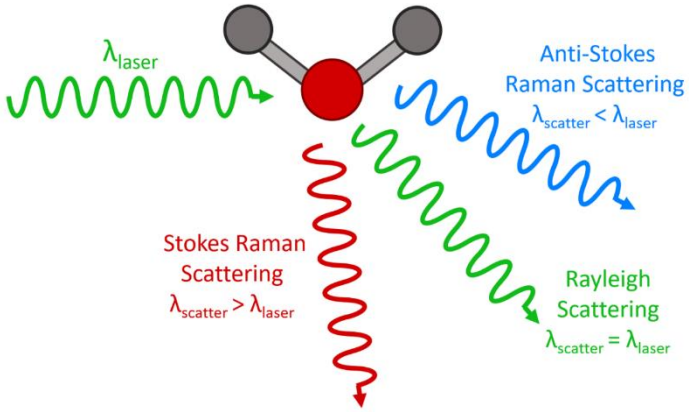

Figure 6: Raman Principle [26].

A Raman spectrum consists of scattered intensity plotted vs. energy. Each peak corresponds to a given Raman shift from the incident light. The Raman spectrum for Si centered at ~520 cm^{-1} is shown in **Figure 7**. This non-destructive characterization technique is used for chemical analysis of a material. With Raman peak, the chemical structure, phase, and crystallinity of the material can be obtained.

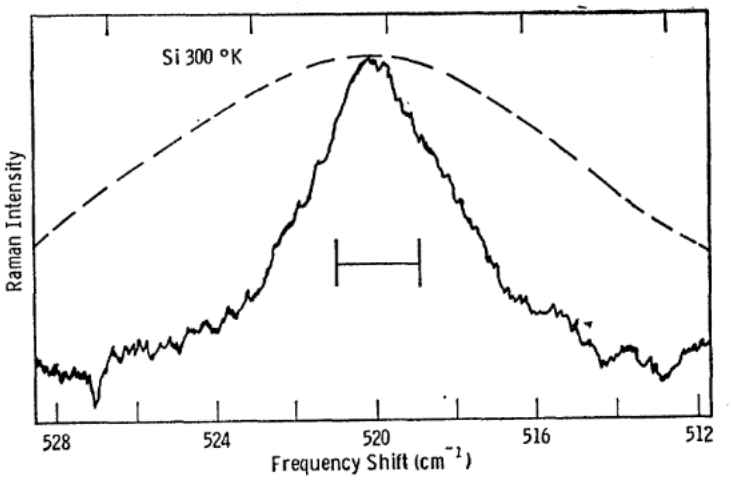

Figure 7: Raman scattering from Si at 300 K [27].

Raman microspectroscopy, or the combination of Raman spectroscopy with an optical microscope offers many advantages for the characterization of Si-based solar cells. The Raman

instrumentation is affordable, no special sample preparation is required, and measurements can be conducted in ambient conditions. The Raman spectrum for Si exhibits a pronounced transverse optical (TO) phonon mode centered at ~520 cm^{-1} which is easily detected [27]. The peak position and full-width-at-half-max (FWHM) are indicators of Si crystalline quality and contain stress information [28]. Compressive stress will tend to stiffen the bond, which leads to a slight increase in vibrational frequency causing Raman shift to the higher wavenumber (superior to 520 cm^{-1}). Other materials used in Si solar cells such as, transparent oxide conductors [29] [30] [31] and interfacial layers of oxides produce their own Raman signal and thus, chemical mapping is possible. Importantly, coupling Raman with confocal measurements (in the *z* i.e., depth direction) can lead to a modality which is non-destructive and provides microscale sub-surface information [32]. Finally, the optics of the microscope and the laser wavelength plays an important role in determining the *x*, *y* and *z* resolution of the measurements and micrometer scale lateral resolution is routinely possible. **Figure 8** shows the schematic representation of the WITec Raman system used.

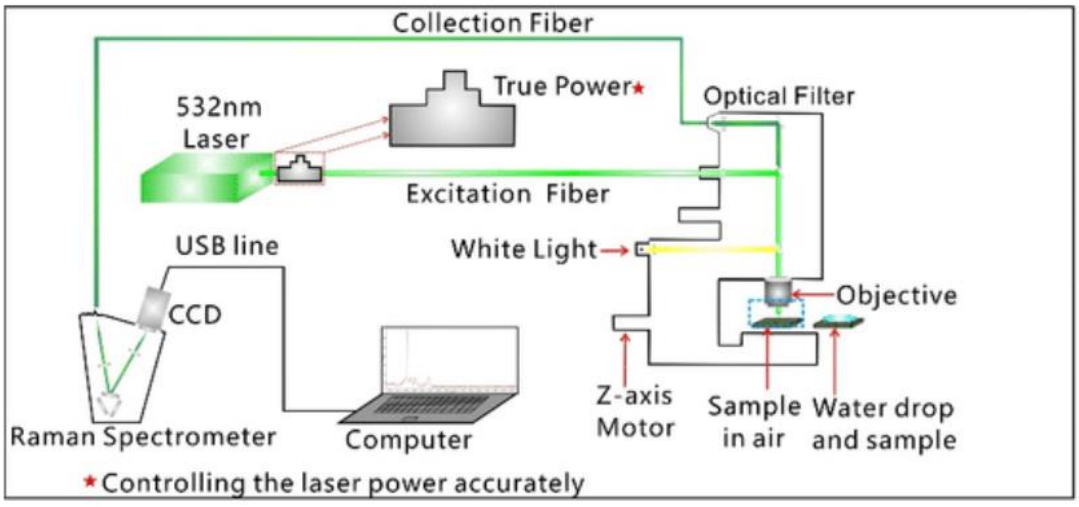

Figure 8: Schematic diagram of the WITec system with optical components and the light path [33].

There have been many seminal articles that provide detailed information of the structure-property relationship in Si. The strong vibration of the transverse optical (TO) phonon peak at 520.5 cm^{-1} in the Raman spectra can be a useful indicator of the distortions in the lattice network and is used to characterize crystalline Si (c-Si). The first-order Si peak is symmetric and has a width of 3 cm^{-1}. As the grain size in crystalline Si decreases, the Raman shift decreases, the width increases, and the peak becomes asymmetric. Raman can also identify small clusters of Si atoms because their structure is different from the crystalline phase [34-36].

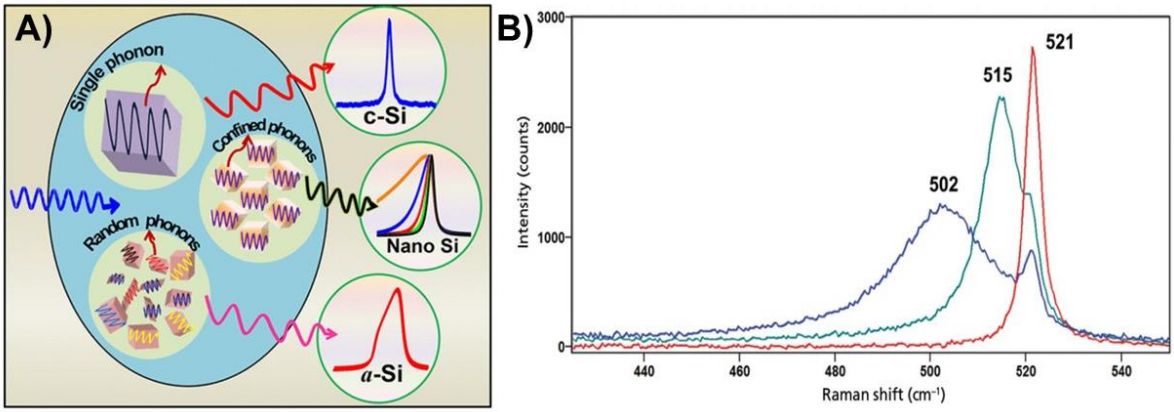

Figure 9: A) Schematic representation of Raman processes involving the scattering from c-Si, nc-Si and a-Si with respective Raman spectra [37]. B) Raman spectra of c-Si (red), microcrystalline and strained Si (green) and nanocrystalline Si (blue)[38].

Raman spectroscopy is highly sensitive to the structure of the Si in its various forms. For crystalline Si the Raman spectrum is centered at 520.5 cm^{-1}. For microcrystalline Si, the Raman spectrum is centered at ~515 cm^{-1}. For amorphous Si (a-Si), the Raman spectrum is centered at 480 cm^{-1}. **Figure 9A** shows the schematic representation depicting various Raman processes involving scattering from single phonon: c-Si, confined phonons: nc-Si and random phonon: a-Si. **Figure 9B** shows the Raman spectra of bulk crystalline Si, microcrystalline Si and nanocrystalline

Si peak. The Raman peak downshifted and broadened from those of bulk Si is attributed to the phonon confinement effect [37].

The laser power plays an important role in Raman spectra. The Raman signal of a Si wafer is a linear function of the laser power [39]. A strong laser power increases the local temperature of Si and affects the Raman spectra. The bulk Si does not show any change because of the poorer thermal conductivity of nano Si compared to the bulk Si. This is shown in Appendix A and C.

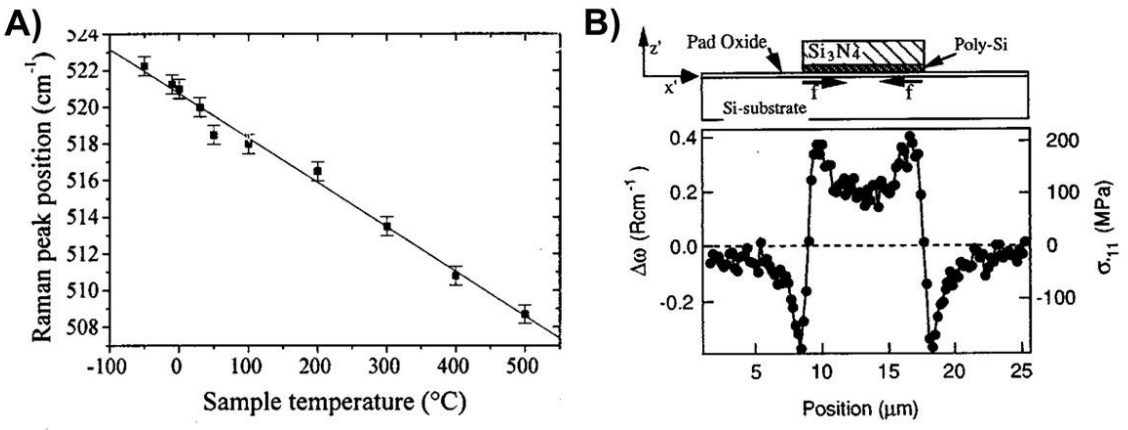

Figure 10: A) Raman peak shift vs monocrystalline Si temperature [40] B) Raman shift and corresponding stress in Si near and beneath a 9.4 μm wide Si_3N_4/poly-Si line. At the top of the figure, a schematic representation of the sample is provided [41].

Raman spectra is sensitive to the local temperature of the Si sample. The Raman peak of Si shifts due to the strong dependency of phonons energy and occupancy on temperature [42]. The variation of monocrystalline Si peak position in accordance with temperature is shown in **Figure 10A**. The increase in temperature leads to a decrease in the TO phonon peak position. With the application of micro-Raman scattering, thermal conductivity in layered materials can be measured nondestructively. Périchon et al., used the relationship proposed by Nonnenmacher and

Wickramasinghe to measure the thermal conductivity of conductors and thin insulating films deposited on top of conductors by thermal scanning probe microscopy. The following were considered: the heat source diameter induces shallow heating, the layer thickness is at least one order larger than the heat source diameter, the distributions of the isotherms within the layer is hemispherical and heat losses in the air are negligible. The thermal conductivity of the layer can be found by the simple linear relationship between the heating power *P* and the local temperature T_j.

$$k_s = \frac{2\,P}{\pi\, a\, \Delta T} \qquad (1)$$

where k_s is the material thermal conductivity, a, the heating source diameter and $\Delta T = T_j - T_b$. T_b is the bulk temperature. With the proposed, the monocrystalline Si thermal conductivity was found to be 63 W/mK at about 550 °C and then applied to porous Si layers. For a 50 µm thick layer with 50% porosity, a thermal conductivity of 1 W/mK was found confirming the thermal insulating properties of this material [40].

Raman spectroscopy provides information on the stress state of Si. With the application of Raman microspectroscopy, micron scale mechanical stress can be characterized in micromachines [43]. This would be reliable and comparable to the commonly used microscale stress measurement methods. Microelectronics structure such as Si_3N_4/poly-Si lines on Si substrate observed through Raman provides mechanical stress information which correlates well with the theoretical stress models. **Figure 10B** shows the schematic representation of a device with Raman shift and corresponding stress in Si near and beneath a 9.4 µm wide Si_3N_4/poly-Si line. The horizontal line shows non stress or zero stress value. In general, a Raman frequency larger than the stress-free

frequency indicates compressive stress in the sample, while a Raman frequency smaller than the stress-free frequency indicates tensile stress. For a (001) Si surface and under biaxial loading condition, the following equation can be used to calculate the stress based on the Raman shift [41].

$$\Delta\omega_3(cm^{-1}) = -4 \times 10^{-9} \left(\frac{\sigma_{xx}+\sigma_{yy}}{2}\right) (Pa) \qquad (2)$$

Investigations on heavily doped P- and B- poly-Si reveals that for a fixed doping concentration, the position of the Raman phonon lines does not change with increasing grain size. In undoped poly-Si, the longitudinal optical-TO phonon line occurs at 517 cm^{-1}, which corresponds to a tensile stress of 750 MPa. The incorporation of B and P dopants causes the phonon peak to shift towards smaller wave numbers. The Raman spectra of heavily doped poly-Si are distorted due to a resonant interaction between optical phonons and direct intraband transitions of electrons and holes in n-type and p-type specimens. Raman spectroscopy of Si has been combined with electrical measurement techniques to provide valuable information on both materials and device quality. For example, highly doped p-type Si in multi crystalline Si solar cells, have been analyzed using a combination of Raman and electrochemical capacitance-voltage measurements. These measurements revealed the free carrier as well as the dopant concentration profiles within the back surface field region was a step-functional shape instead of the extended gradient shape which the electrochemical capacitance-voltage measurements suggest [44]. As for the electrical characterization of photovoltaic devices, the Raman Si crystallinity plays an important role. Microcrystalline Si single-junction solar cells investigated through Raman and electrical investigations show the open-circuit voltage linearly decreases as the average of the Raman crystallinity factors . Raman crystallinity factor indicative of crystalline volume fraction is

introduced and applied to the interface regions, i.e. to the mixed amorphous-microcrystalline layers at the top and at the bottom of entire cells by top and bottom illumination [45].

While there are obvious advantages of combining Raman with electrical measurements, additional instrumentation requirements limit the widespread adoption of the aforementioned techniques. One possible approach which can reduce the burden of additional instrumentation is by recognizing that the laser of the Raman system can be used to photoexcite carriers in the semiconductor thus mapping the current generated, simultaneously. The measurement of photocurrent with a rastering laser beam is termed as LBIC and, combined with Raman can provide an integrated instrumentation platform linking semiconductor materials properties with device characteristics. Thus, combined Raman and LBIC methodology provides an easy and integrated system where no additional hardware is needed to conduct the LBIC part of the test other than for extracting the photocurrent.

3.3 Laser Beam Induced Current

LBIC measurement is a non-destructive characterization technique used for testing the electrical quality of semiconductors. A light beam is scanned over the surface of a photosensitive semiconductor device creating electron-hole pairs. If the electron-hole pairs can be separated (via internal or external electric fields), then the photocurrent generated can be measured. This photocurrent is a strong function of the electrical quality of the semiconductor. High quality semiconductors and devices thereof can generate high photocurrents. On the other hand, semiconductors which have defects and impurities including unpassivated surfaces, inclusions and grain boundaries lead to a loss of photocurrent. Measurements are repeated for various positions

of the laser beam to produce an LBIC image of the device. Variations in the measured current is converted to variation in contrast to form an LBIC image indicating electrically active and inactive areas. LBIC is used as a quality control tool from module to cell level in inline diagnostics of solar cells. A basic LBIC system set up is show in **Figure 11**.

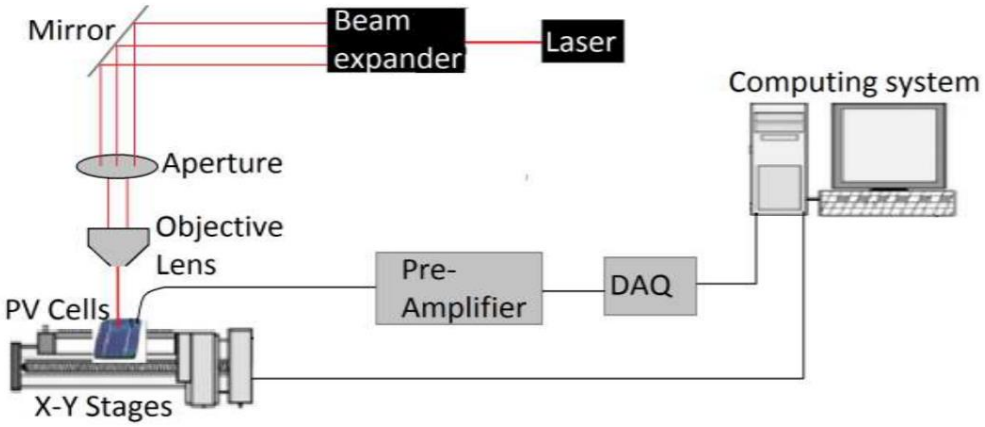

Figure 11: LBIC measurement set up [46].

A brief literature review on LBIC on photovoltaics categorized into first generation, second generation and third generation solar cells is given below. **Figure 12A** shows the solar LBIC map at zero cell bias of a multi crystalline Si solar cell [47]. The figure shows the cracked edge of the cell as well as the manufactured edge of the cell. The drop in induced current is ascribed to the reduced shunt slope at the original manufactured edge.

The LBIC technique has been implemented in research as well as in production. There have been research on LBIC modeling with multiple assumptions. Marek et al., presented a three-dimensional calculation of LBIC currents at grain boundaries (GBs) modeled as a two-dimensional plane of recombination centers [48]. Considering the surrounding semiconductor to be homogenous and a minority carrier diffusion length, a light beam with finite width resulted in a finite lateral extent of the pair-generation volume and allowed to widen with increasing depth due

to the divergence of the beam. The depth dependence of the generation considered to be exponential to the absorption coefficient. With the above considerations, the experimental LBIC data on crystalline solar cells obtained at various wavelengths agreed with the theoretical predictions.

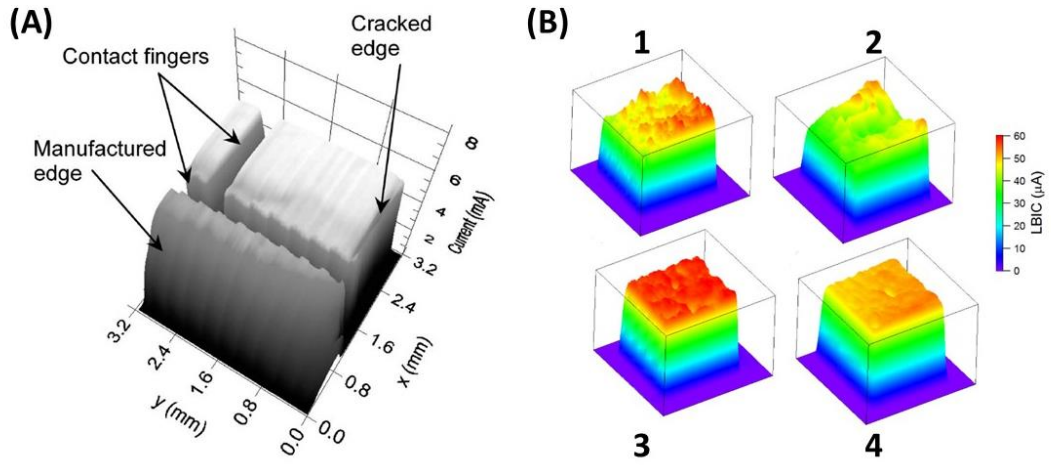

Figure 12: A) Solar LBIC map at zero cell bias over an area of 3.2 × 3.2 mm2 on the corner of a cracked flat plate multicrystalline Si cell [47] B) LBIC maps of perovskites devices prepared by 1)single step spin 2) single step spray 3) sequential spins and 4) sequential spray/spin methods [52].

LBIC has been used to show that porous Si layer treatment of crystalline Si solar cells can passivate both the grains and grain boundaries. LBIC mapping revealed that the layer treatment improved the quantum response and reduced the grain boundaries activity. Because of the improvement of the minority carrier diffusion length and the passivation of recombination centers at the boundaries, there was an LBIC enhancement. The internal quantum efficiency (IQE) range shifted from 47 - 48% to 46 - 64% after the treatment, thus leading to high-efficiency crystalline Si solar cells [49].

Leite et al., studied CdTe/CdS solar cells to map the photocurrent generated at GBs under different illumination conditions. The study revealed that the GBs were very efficient current collectors and can be resolved by LBIC microscopy. Cross-sectional measurements showed a clear dependance of the GBs transport properties with distance from the junction.

Probing devices under forward bias (V_{OC}) is also possible and can be expanded to other materials. This local measurement of the photoelectronic properties of GBs in thin-film CdTe solar cells by LBIC is an important step to understand how GBs impact the device performance and to map the diffusion length and recombination rates of the GBs that can be used to engineer a device with enhanced V_{OC} [11].

Musca et al., used LBIC technique to extract fundamental material and device parameters for photovoltaic Mercury Cadmium Telluride (HgCdTe) devices. The LBIC signal was shown to be strongly dependent on a number of material and device parameters such as surface recombination, diffusion length and surface recombination velocity thus showing LBIC, the candidate to characterize HgCdTe devices. Molecular-beam epitaxy (MBE) grown HgCdTe includes growth regime of voids, triangles and microvoids. These features affect the performance of devices fabricated within the vicinity of defects. Not all defects are electrically active such that they provide a current leakage path to shunt the p-n junction of the individual photodiode.

LBIC as n nondestructive technique has been used to characterize the electrically active defects in photodiodes arrays. The presence of a single leakage path within the p-n junction can produce a vertical shift of the LBIC profile depending on the location along the junction of the device structure. This can be used as an indicator to confirm the presence of the localized leakage

in most situations. Thus, LBIC can be used as a screening tool for focal plane array production lines [50, 51].

LBIC has also been employed in characterizing perovskites and polymer solar cells to study the relationship between the solution processing method and the resultant morphology, film uniformity and device performance. In situ degradation study of perovskite solar cells under high humidity conditions is possible and can be performed through LBIC mapping. Perovskites decompose in the presence of water and degrades when exposed to intensive light. The LBIC study on devices with different perovskite absorbers and hole transport materials identified different degradation mechanisms that can be used to improve device stability. **Figure 12B** shows LBIC maps of perovskite devices prepared by various techniques. Single step coating (1 & 2) shows less uniform LBIC signals than devices prepared by sequential methods (3 & 4). The loss of Methylammonium iodide (MAI), a precursor used in preparing the device, causes the formation of voids and defects during the annealing step [52].

Dye sensitized solar cells (DSSC), a type of photovoltaic cell based on a solid-liquid interface are easier to make and cost less expensive. The application of LBIC technique in characterizing DSSC was uncommon because of their configuration. In contrast to solid-solid interfaces, DSSCs show a slow response to irradiance variations providing diffused images. Francisco et al., presented a method to produce high resolution LBIC images of DSSCs using an algorithm based on the kinetics of the discharge process of the irradiated zone. The method has been experimentally used in obtaining more reliable information about relationship between the structure of the cell and its conversion efficiency [53].

LBIC has been widely used in semiconductors and photovoltaics to investigate non-uniformities and defects. LBIC is very reliable, practical and can show differences in process variations. The monochromatic light source is the commonality in both the instrumentation. By using the light source from the Raman microspectroscopy instrumentation and with the addition of an external data acquisition system for collecting the charge carriers, synchronous micron-Raman and micro-LBIC can be performed. This will eliminate the need of instruments such as Photovoltaic analyzer PVScan 5000, sample preparation and the cost. Structural defects will be identified through Raman and electrically inactive areas will be characterized through LBIC in a single modality.

CHAPTER FOUR: INSTRUMENTATION

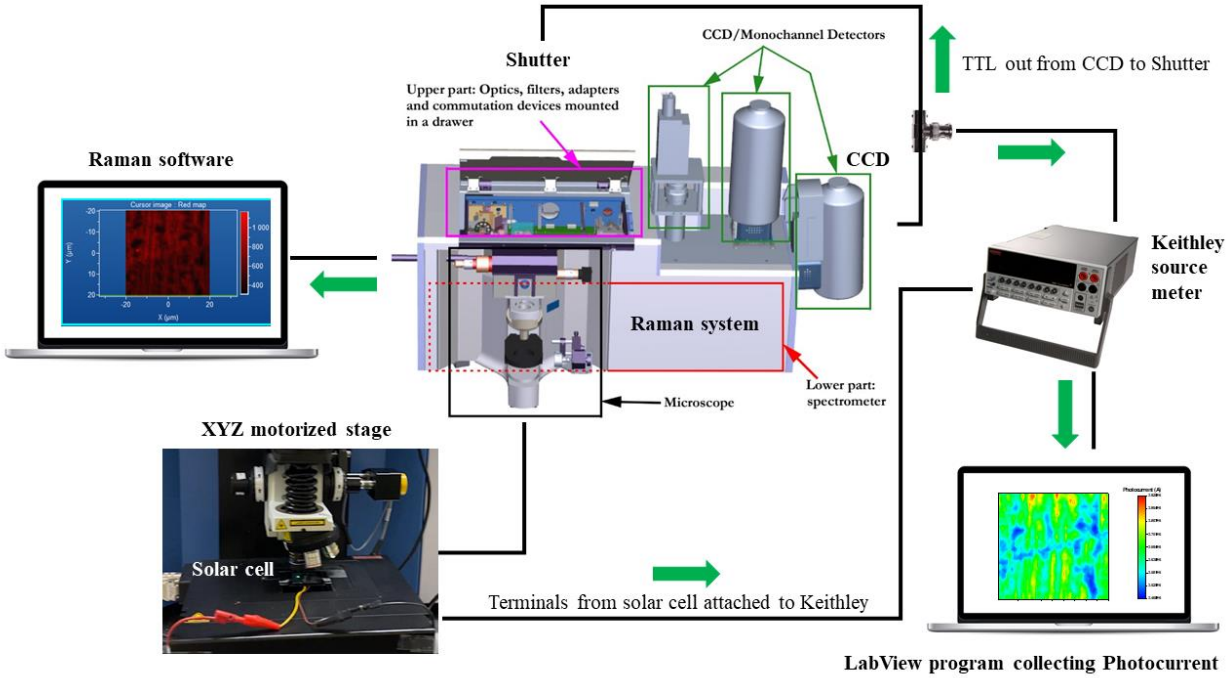

Figure 13: Synchronous Raman and LBIC measurement setup.

The above figure shows the synchronous Raman and LBIC measurement setup. As mentioned earlier, the central hypothesis of the work is that the laser source used for performing Raman studies can be used simultaneously to measure LBIC for any photonic device. To successfully integrate the LBIC measurement module using the Raman system laser, a custom built LabView program was used. The program controls the Keithley source meter to collect photocurrent generated from the solar cell. The Keithley meter is connected to the Transistor-transistor logic (TTL) out cable from the Charge-couple device (CCD) to the Shutter. The synchronous measurement is possible by using the Raman system to trigger the source meter to measure current when required. The motorized XY stage moves to measure the Raman areal mapping based on the users XY coordinates. As it moves from one point to another, the CCD will

send out the TTL pulse signal to open shutter at each acquisition. Since the Keithley source meter is connected to the TTL out, it measures photocurrent when triggered. With this setup, the photocurrent collected by the LabView program is very well synchronized with the Raman measurement thus, matching the Raman and LBIC measurements spatially in a solar cell.

CHAPTER FIVE: RAMAN MICROSPECTROSCOPY OF A MULTICRYSTALLINE SILICON SOLAR CELL

The contents of this chapter have been published in: J. P. Ganesan, N. Iqbal, M. Krsmanovic, F. Torres-Davila, A. Dickerson, K. O. Davis, L. Tetard and P. Banerjee, "Raman microspectroscopy of a multi-crystalline silicon solar cell", IEEE Journal of Photovoltaics, 2022.

5.1 Materials

Multi crystalline aluminum back surface field (Al-BSF) solar cell was obtained from Canadian Solar®. From top to bottom, the layers were Ag contacts, a 75 nm SiN_x layer as an anti-reflecting coating (ARC), *n*-type Si as emitter, 180 µm *p*-type Si absorber and a thick 250 µm thick Al back contact. The methodology is provided in **Appendix A**.

5.2 Results and Discussion

Figure 14A shows the surface image of the multi crystalline solar cell. The presence of Si nitride (Si_3N_4) as an ARC makes the surface appear blue in color. Screen printed Ag fingers are approximately 2 mm apart. Regions marked on this image were analyzed using Raman microspectroscopy and will be described next. Region 'B' is the approximate region where remnants of saw marks were visible. Region 'C' indicates the Ag finger on the solar cell coupon. Region 'E' marks the presence of an inclusion found on the Si surface between two Ag fingers.

Figure 14B shows the saw mark region 'B'. These saw marks appear to run parallel to each other, characteristic of the wire-saw based process employed for wafering. Usually, saw marks are removed during the surface texturing process. However, in this case, a small region (~2 mm^2) still shows remnant saw marks on the multi crystalline Si surface. **Figure 14C** shows the top down

and, **Figure 14D** shows the profilometric cross-section of the Ag finger. The cross-section of the Ag finger is approximately rectangular in shape. The fingers are ~ 30 μm wide and ~ 10 μm tall. The sidewalls are slightly tapered with an angle of 60°. Next to the sidewalls there appears to be a planar, 'spill-over' region that has leftover Ag from the firing process which is described in detail below. **Figure 14E** and **Figure 14F** shows the optical profilometry image of the inclusion present on the Si surface. The inclusion measures 20 μm in the *X* direction, 45 μm in the *Y* direction.

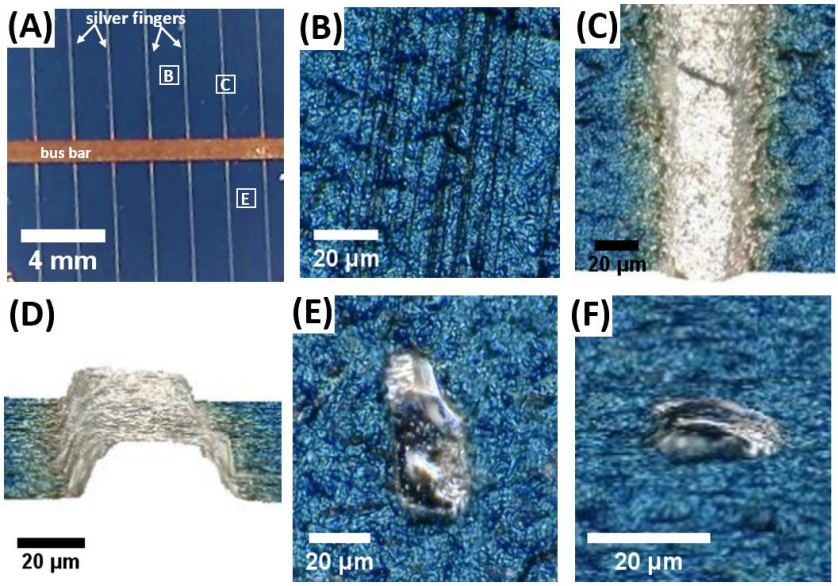

Figure 14: (A) Surface image of a multi crystalline solar cell. Bus bar and Ag fingers are labelled. Regions marked B, C and E correspond to approximate regions for scratch mark, Ag finger and inclusion, respectively. (B) Optical profilometer image of scratch marks. (C) Optical profilometer image of Ag finger. (D) 3D cross-section of the Ag finger region. (E) Optical profilometer image of inclusion and (F) 3D cross-section image of the inclusion.

Figure 15A shows the Raman spectrum obtained on the multi crystalline Si solar cell surface. The TO phonon peak is centered at 520.3 cm^{-1}. The inset shows the micrograph of the textured Si surface acquired under the microscope at a magnification of 20×. The 25 × 25 μm^2 red

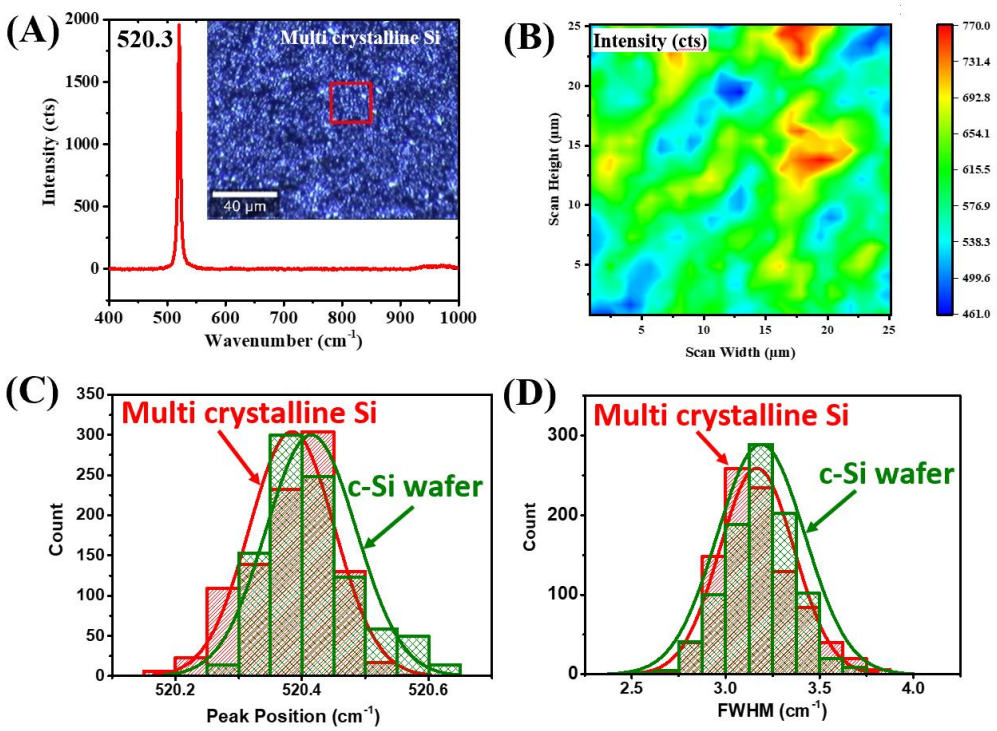

Figure 15: Si Raman spectrum of the TO phonon peak centered at 520.3 cm-1. The inset shows the surface of the textured multi crystalline Si solar cell surface. (B) Intensity map of a 25 x 25 mm2 red box from (A) which contains 961 data points. (C, D) Histogram distribution of peak position (C) and FWHM (D) of the multi crystalline Si compared with a single crystal.

boxed region is mapped next. **Figure 15B** shows the *XY* contour plot of the variation of Raman peak intensity. The variation in intensity on the multi crystalline Si surface is attributed to the texturing process that causes the variation in the Si surface topology. Thus, regions in the plane of focus cause higher peak intensities. Regions away from the plane of focus (either above or below) cause lower peak intensities. The distribution of the peak position in a 25 x 25 μm^2 area is shown in **Figure 15C**. A MATLAB® code was written to extract the peak position and FWHM using a Lorentzian fit. Recall that a total of 961 data points were acquired for this area scan. The peak position varies from 520.2 cm^{-1} to 520.6 cm^{-1} and follows a Gaussian distribution. The peak

position distribution of a multi-crystalline solar cell is overlayed over the peak position distribution of a pristine, single crystal Si wafer and appear to be very similar. The similarity in the distributions indicate similarity in the crystalline quality of Si between both samples. Since peak positions are also indicative of mechanical stress in Si [41], these results indicate that the multi-crystalline Si is stress free in the red boxed region of **Figure 15C**. As a further confirmation of this conclusion, in **Figure 15D** the variation of full width at half maximum (FWHM) of the Si peak is overlayed over the variation of FWHM of the pristine single crystal Si wafer. This variation is found to be in the range 2.7 cm^{-1} to 3.8 cm^{-1} for both samples. Polycrystallinity and GB effects were not observed on the multi-crystalline Si surface.

Figure 16A shows the micrograph of saw marks present on the Si. As stated before, the saw marks are suspected to be remnants of an incomplete etching and texturing process which otherwise should have removed the imperfections from the surface. The red boxed region measuring 75×25 μm^2 was mapped under the Raman microscope next. **Figure 16B** shows the *XY* contour plot of the intensity of the Si. It is interesting to note that the saw marks do not register on the intensity plot. This is possibly a result of the textured surface determining the surface topology of the multi crystalline Si. **Figure 16C** and **Figure 16D** show the distribution of the peak position and the FWHM of the Si peak, respectively. A MATLAB® code was written to extract the peak position and FWHM using a Lorentzian fit. These are overlayed with the distribution of peak position and FWHM from the multi crystalline textured Si shown in in **Figure 16C** and **Figure 16D**. It is important to note that since the areal mapping of the saw marks region is larger (75×25 μm^2) than the region without saw marks evaluated previously in **Figure 15** (25×25 μm^2), the histogram for the saw marks were sampled to match the size of the evaluated region without saw

marks i.e., 25 × 25 μm^2 = 961 data points. Both the peak position and the FWHM are shifted to a higher value for the saw marks region, indicating that in the presence of the saw marks the Si is under compressive stress. Similar Raman shifts indicating residual compressive stress have been reported when analyzing Si swarf from the sawing process [54]. Further, the peak position and FWHM distributions are wider for the saw marks region. FWHM are an indicator of the crystalline quality of the Si and performing statistical analysis of Raman data helps to delineate these differences.

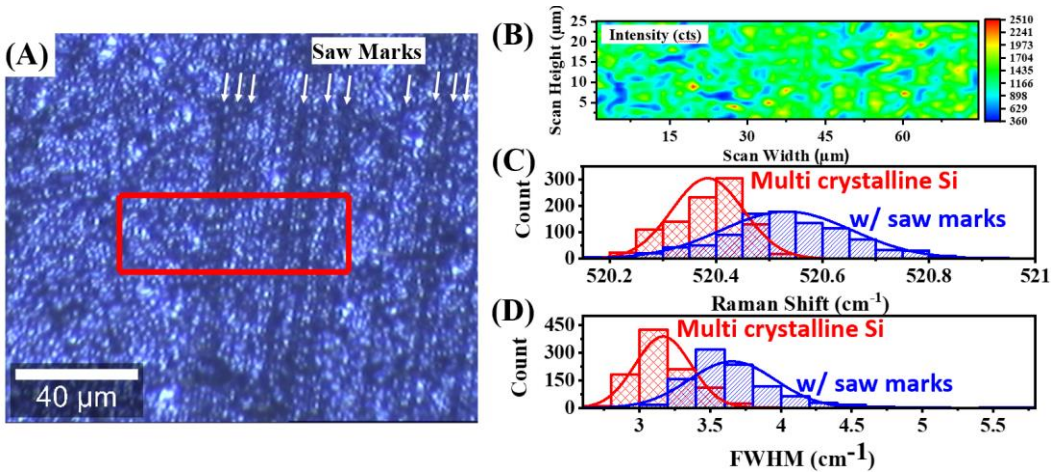

Figure 16: (A) Region of Si solar cell indicating saw marks. The 75 x 25 μm^2 red box is the region in which Raman mapping was conducted. (B) Contour plot of Raman intensity shows no indication of the saw marks. (C, D) The distribution of peak position (C) and FWHM (D) from area mapping for multi crystalline Si only and Si with saw marks regions.

Figure 17A shows a single Raman spectrum at the edge of the Ag finger shown in the inset with a '+' mark. The spectrum consists of two peaks. The primary peak is the TO phonon belonging to Si at 520.3 cm^{-1} and the weaker, broader peak is at 680 cm^{-1}. The peak at 680 cm^{-1} is attributed to the vibration of $Ag[O\text{-}O]^{2-}$ bond in Ag_2O [55]. The origin of Ag_2O can be attributed to oxidation of Ag during the firing process [56, 57].

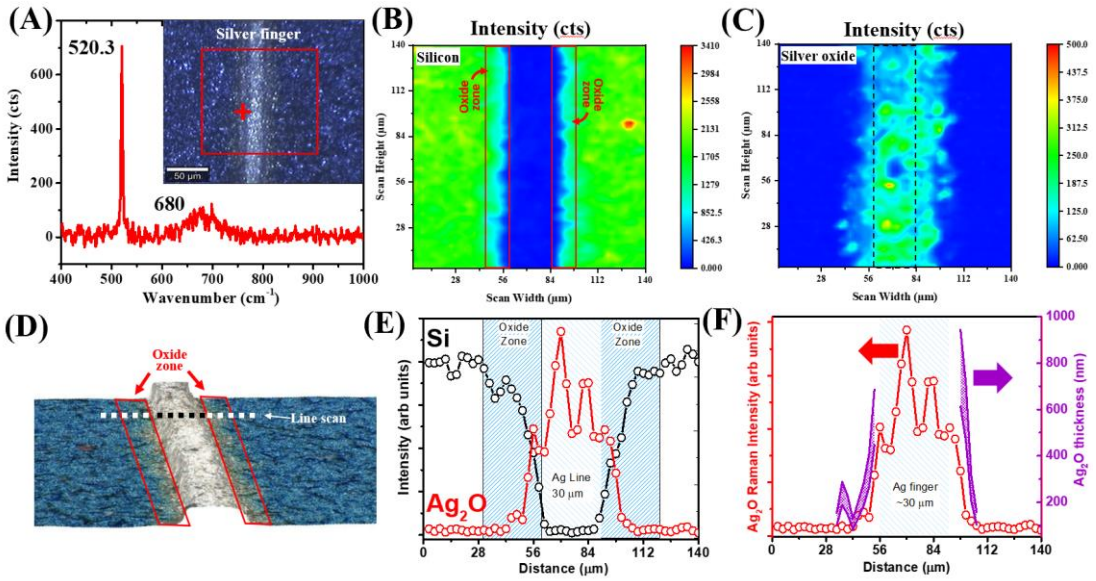

Figure 17: (A) Raman spectrum of the silver line on the '+' mark in the inset shows two peaks – one at 520.3 cm^{-1} corresponding to the underlying Si and another, weaker peak at 680 cm^{-1} which corresponds to Ag_2O. (B) Contour plot of the intensity of 520.3 cm^{-1} peak shows the presence of Si around the silver line. The 'oxide' zone is labeled which shows diminished Si intensity. (C) The intensity of the 680 cm^{-1} peak is shown which appears concentrated above and in the vicinity of the silver line. (D) 3D profilometer image shows the oxide zone and the dotted lines are approximate positions of representative Si and Ag_2O line scans which are provided as intensity plots in (E) and (F), respectively. From the drop in Si intensity and, assuming the absorption coefficient for Ag_2O to lie between 0.00078 and 0.0012 nm^{-1} it is possible to estimate the thickness of Ag_2O in the oxide zone.

Figure 17B shows the areal mapping of the Si peak intensity from the red boxed region in the inset of **Figure 17A**. At distances ≥ 15 μm from the edge of the Ag line, the Si peak intensity is relatively uniform. As the laser approaches the Ag line, the Si peak intensity starts to decrease. Once the laser is atop the Ag line, the Si peak disappears completely, as expected. Our region of interest is in the transition region where the Si peak intensity gradually decreases. Here, we note that since the laser spot during the raster does not overlap with the previous spot, the information

obtained at any given *XY* coordinate is expected to be free of neighboring site effects and thus, signal deconvolution is not needed. The drop in intensity of Si can thus be attributed to compositional changes occurring at the site of interest.

The drop in Si peak intensity is attributed to residual Ag_2O on the surface which absorbs part of the laser intensity. The region is highlighted in **Figure 17B** as an ‘oxide zone'. This is not unreasonable since Ag_2O has a band gap of ~2.50 eV [58] and is likely to absorb a certain fraction of photons at a wavelength of 532 nm (i.e., photons with energy, 2.33 eV).

To establish the idea of an oxide (i.e., Ag_2O) zone which is wider than the Ag line, we plot the Ag_2O peak intensity as an area map in **Figure 17C**. The dotted lines indicate the edges of the Ag finger and, where the Si peak intensity reaches zero. Clearly, the Ag_2O is detected well beyond the Ag line. Additionally, in **Figure 17D** we highlight the 3D optical profilometry results of the Ag line. The oxide zone appears as a discolored region neighboring the Ag line.

A line scan is conducted on the Ag line as indicated in **Figure 17D**. The data is plotted in **Figure 17E**. As mentioned previously, the Si peak intensity drops while approaching the Ag line. Simultaneously, the Ag_2O peak intensity increases in value. Along the Ag line, where the Si intensity is nearly zero, the Ag_2O peak intensity varies depending on the thickness of oxidized Ag on the surface of the finger.

We use the following approach to estimate the thickness of the Ag_2O left behind in the oxide zone. First, we assume that the Si peak intensity is a linear function of the laser intensity [39]. That is, the drop in the Si peak intensity is directly proportional to a corresponding drop in the laser intensity. Thus,

$$\frac{{I_{Raman,Si}}^{max}}{{I_{laser}}^{o}} = \frac{I_{Raman,Si}}{I_{laser}} \qquad (3)$$

where , ${I_{Raman,Si}}^{max}$ the maximum Raman intensity of Si obtained at a laser intensity of ${I_{laser}}^{o}$ (30 mW), $I_{Raman,Si}$ is the Raman intensity of Si at a given coordinate *XY* with laser intensity I_{laser} (< 30 mW). According to **equation *1***, if the laser intensity decreases due to absorption from an overlying film there will be a proportional decrease in the Si Raman peak intensity.

We further assume the drop in laser intensity is due to absorption in the Ag_2O layer. This allows one to apply Beer-Lambert's law to estimate the thickness of Ag_2O film ('z') in the oxide zone. This is given as,

$$I_{laser} = I^{o}_{laser} e^{-\alpha z} \qquad (4)$$

where α is the absorption coefficient and *z* is the thickness of the oxide. In **equation *2***, I_{laser} is obtained from equation *1*. To apply Beer-Lambert's law to estimate *z*, the absorption coefficient of Ag_2O at 532 nm must be known. Unfortunately, in literature the absorption coefficient of Ag_2O is rather uncertain. Heat-treated Ag_2O films have an absorption coefficient at 532 nm in the range 0.00078 to 0.00122 nm^{-1} [59]. Thus, these two values serve as the upper and lower limit of the absorption coefficient. Because of the range of the absorption coefficient, the estimated thickness *z* of the Ag_2O film can, at best, be estimated within a range.

The result of this approach is shown in **Figure 17F**. For clarity of understanding, the original Ag_2O Raman peak intensity is plotted again on the left-*Y* axis and is the same data plotted in **Figure 17E**. This plot provides the ${I_{Raman,Si}}^{max}$t large distances from the Ag line edge) and $I_{Raman,Si}$. Overlaid on this plot are the estimated Ag_2O film thickness range as obtained using the

upper and lower values of absorption coefficient from **equation *2***. The thickness data shows that up to ~ 200 nm of Ag_2O can be found 25 μm away from Ag lines.

One possible reason for the presence of the Ag_2O up to 25 μm away from the lines could be the initial application of Ag paste during the screen-printing process. The Ag paste application may have a lateral spread greater than the targeted line width (~ 30 μm) obtained after the firing step. During the firing process, the volatile components are removed from the paste while the metallic components sinter and shrink laterally leaving residual Ag_2O behind.

In **Appendix C**, we provide the scanning electron microscope energy dispersive x-ray spectroscopy (SEM EDX) data of a similar, Ag line with elemental mapping. Of particular interest is the O- map which clearly detects O beyond the width of the Ag line. This adds further support to the claim of detecting Ag_2O on multi crystalline Si surfaces using Raman. In **Appendix D**, x-ray photoelectron spectroscopy (XPS) of the Ag line is presented, showing a Ag^+ shoulder on the 3d peaks. XPS indicates ~15 at % oxide on the surface of Ag lines. These data add further support to the claim of detecting Ag_2O on multi crystalline Si surfaces using Raman.

Figure 18A shows a micrograph of an inclusion as seen under the Raman microscope. This inclusion is previously shown in **Figure 14E** and **Figure 14F** as profilometry images. Recall that the 3D image appears to show this inclusion embedded inside the multi crystalline Si surface. A line scan was conducted from $X \rightarrow X'$. In **Figure 18B**, a series of twelve individual Raman spectra are sampled from X (at the bottom) to X' (at the top). Each scan is 1.6 μm apart. At point X just outside the inclusion, the scan consists of a sharp peak at 520.3 cm^{-1} assigned to crystalline Si (c-Si). As the scan position moves over the inclusion, an additional broad peak appears on the lower wavenumber side. As the probe moves over the inclusion the peak position changes from

504.0 cm^{-1} to 492.0 cm^{-1}. Approaching *X′*, the broad peak subsides, and the c-Si peak sharpens again.

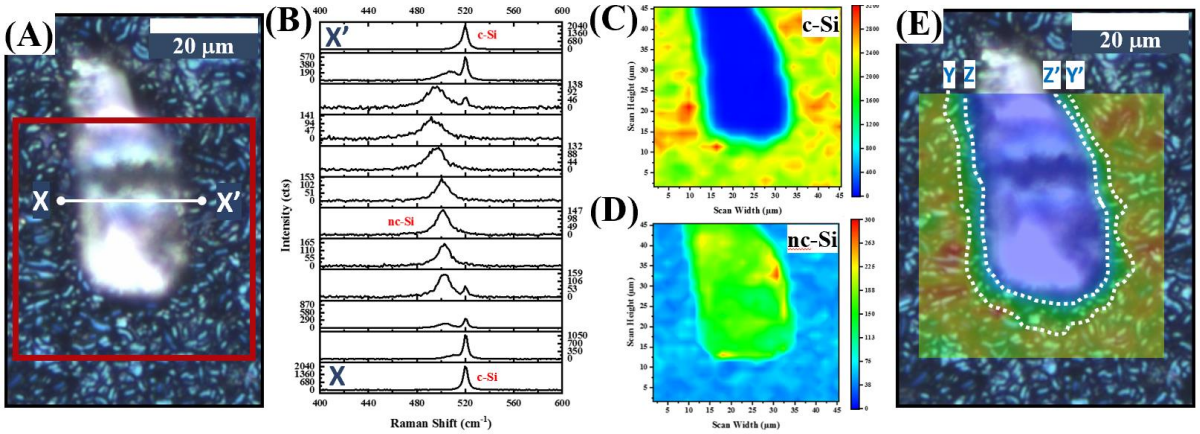

Figure 18: (A) Microscope image of inclusion with XX′ showing the line scan and red box indicating the area scan. (B) A series of twelve spectra taken across XX′ showing the transition from c-Si to nc-Si and back to c-Si. (C) XY mapping of the peak intensity for c-Si (D) XY mapping of the peak position for nc-Si. The color scale shows the intensity. (E) c-Si peak intensity from (C) overlayed on the microscope image from (A) showing the interfacial region between YY′ and ZZ′.

Peak shifts to lower wavenumbers in the TO phonon mode of the Si result from i) tensile stress, ii) phonon confinement due to nanocrystallinity or, iii) temperature changes to the sample. In the case of nanocrystalline Si (nc-Si), these effects are complex. This secondary Si peak belongs to nc-Si which lies between c-Si (520.3 cm^{-1}) and the fully amorphous Si (a-Si) peak at 480.0 cm^{-1} [60, 61]. Based on past work, the inclusion represents a Si swarf – a possible remnant of the Si ingot sawing process [54, 62]. Here, the c-Si is converted to nc-Si due to the extreme stresses involved during sawing.

To confirm the presence of the nc-Si phase, the Raman peak intensity was measured as a function of the laser power for, 1) c-Si adjacent to the inclusion, and 2) the nc-Si inside the

inclusion. This data is shown in **Appendix E**. For c-Si, the peak position and FWHM does not vary as laser power varies from 0.87 to 24.3 mW. This is expected since, as shown in **Appendix B**, the temperature rise at 10 mW in Si is negligible. On the other hand, the peak position and FWHM of nc-Si is a strong function of laser power. At very low laser power (0.87 mW), the peak position and FWHM match that of c-Si. However, with increasing laser power (4.4 mW and higher), the peak position drops to lower wavenumbers and the FWHM increases.

The decreasing wavenumber of the Raman peak associated with the inclusion can be explained based on the different thermal conductivities (k_s) of c-Si and nc-Si. Room temperature bulk Si k_s is 150 W/m K whereas, recent *ab initio* results matching experimental data indicate nc-Si with 20 nm grain size can exhibit a k_s = 8.4 W/m K; a 17.8× reduction compared to bulk c-Si [40, 63]. The difference in thermal conductivity is a result of the high GB scattering of phonons in nc-Si [64] indicating that heat dissipation in nc-Si is significantly reduced, producing higher temperatures as compared to c-Si, under the same laser power. Thus, the peak position and FWHM is a strong function of laser power in nc-Si.

The peak intensity of the c-Si and nc-Si phases at laser power 25 mW are mapped in **Figure 18C** and **Figure 18D**, respectively. The areal mapping is obtained from the red boxed region in **Figure 18A**. Here the c-Si peak is found to vary from 520.4 cm^{-1} to 519.3 cm^{-1}, indicating tensile stress around the inclusion [41]. The broad nc-Si peak, on the other hand, varies from 511.2 cm^{-1} to 492.0 cm^{-1}. A significant aspect of these areal maps is that the c-Si peak intensity reduces in its value at least 2 - 5 μm away from the observed physical edge of the inclusion. At the same time, the nc-Si peak intensity increases. Thus, the coordinates for which the c-Si peak intensity reduces,

and nc-Si has non-zero peak intensities appear to occupy an area much larger than the physical dimensions of the inclusion.

The above effect cannot be an artifact of measurement at phase boundaries usually associated with raster-based mapping techniques under a microscope. There are two reasons for this. First, the laser spot size of 800 nm (for 10× objective) is less than the width of the observed transition region of 2 – 5 μm. This implies the spatial resolution of the measurement exceeds the feature size observed. Second, the raster step of 1.6 μm is programmed to ensure any two neighboring laser spots do not overlap with each other. This avoids signal convolution from neighboring spots.

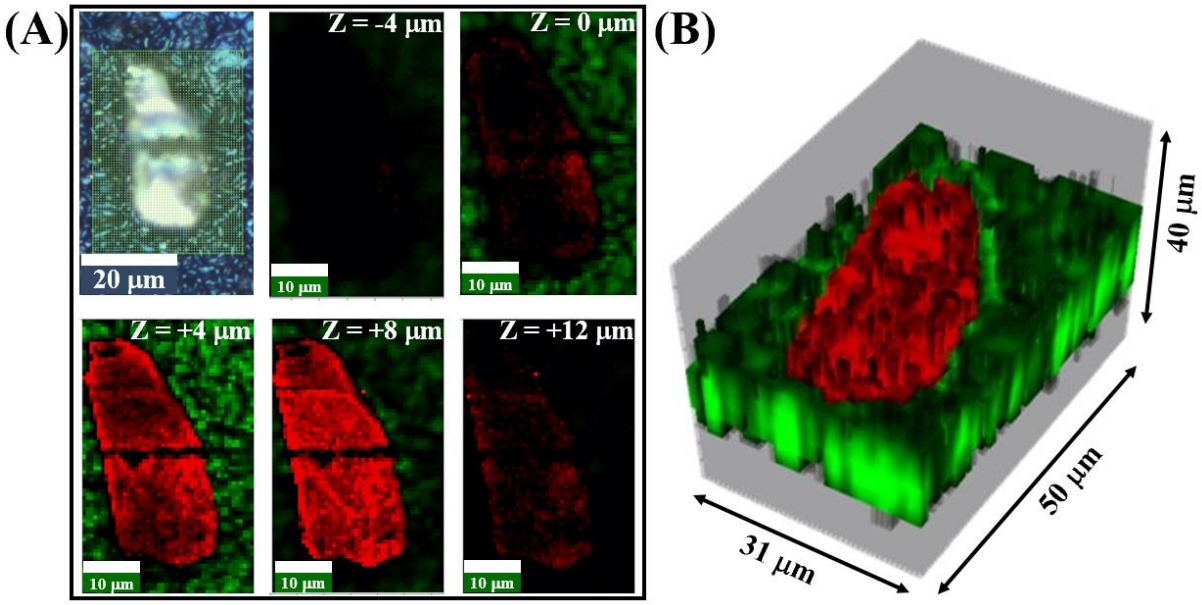

Figure 19: (A) Top left shows the microscope image of an inclusion with the scan area used for confocal imaging. Confocal XY scans at various Z depths (-4 μm ≤ Z ≤ + 12 μm) of the inclusion are shown. (B) 3D Raman reconstruction of the inclusion. Note: green region is Si and red region is nc-Si.

The peak shift to the lower wavenumber for c-Si indicates tensile stress around the inclusion. While the formula for estimating the stress is known under a biaxial state of stress [41], we refrain from calculating this stress due to the complex shape of the inclusion itself. This transition zone is mapped in **Figure 14E** over the original microscope image of the inclusion. The region between the borders *YY′* and *ZZ′* indicates the region where the c-Si is under tensile stress and suggests that the inclusion consisting of nc-Si interacts strongly with underlying c-Si substrate.

The inclusion described above was subjected to confocal Raman mapping as it provides a non-destructive technique for observing sub-surface structure and obtain a 3D map of the inclusion. Confocal mapping was done with a 785 nm laser that, as stated before in the experimental section, allows for a penetration depth of 10 μm and is ideally suited for confocal microscopy in Si. The results are shown in **Figure 19A** as a series of *XY* intensity plots for different *Z* heights. At $Z = -4$ μm, the laser cannot detect any part of the Si solar cell. As the sample height is dropped (i.e., focal plane of the laser raised) by 4 μm to $Z = 0$ μm, both the Si substrate and the inclusion can be seen.

The green color corresponds to the c-Si peak ($519.0\ cm^{-1} \leq \omega \leq 520.5\ cm^{-1}$) while the red corresponds to the nc-Si ($492.0\ cm^{-1} \leq \omega \leq 511.0\ cm^{-1}$). Intensities for both Si substrate and the inclusion increase for $Z = +4$ μm and the inclusion can be clearly seen at this *Z* height. The dark band through the middle was a result of using a high power from the laser that led to partial damage of the inclusion. Further increasing the height to $Z = +8$ μm shows the inclusion but does not illuminate the substrate in equal proportion, implying that the focal plane of the laser lies beyond the DOF of the objective and above the Si surface. This observation is in line with the profilometry image (**Figure 14E** and **Figure 14F**) which shows the inclusion to protrude beyond the Si solar

cell surface. Furthermore, the confocal data identifies the inclusion as nc-Si. Finally, at Z = +12 μm the laser focal plane is far removed from both the inclusion and the Si substrate and are barely detected via mapping. These individual maps can be vertically stacked and represented as a 3D image as shown in **Figure 19B**, clearly highlighting a nanocrystalline inclusion embedded on a Si solar cell surface. Thus, confocal Raman microspectroscopy can be a powerful, non-destructive metrology tool to evaluate features in 3D as well as probe sub-surface features in Si solar cells.

5.3 Conclusion

Raman microspectroscopy has been used successfully used to characterize multicrystalline Al-BSF Si solar cell. Four prototypical regions were scanned and analyzed. The results demonstrate the utility of Raman microspectroscopy in obtaining insights into the surface and sub-surface quality of Si solar cells, defect detection and characterization.

CHAPTER SIX: RAMAN MICROSPECTROSCOPY OF A DAMP HEAT TESTED MULTICRYSTALLINE SILICON SOLAR CELL

6.1 Materials & Methodology

A damp heat tested solar cell of the same configuration as explained in Chapter 5.1 was used. **Figure 20** shows the fresh and damp heat tested solar cell. The bus bar on the damp heat tested cell is peeled off. Damp heat (DH) test consist of leaving solar cells in chamber at 85 °C and 85 % relative humidity for several hours. Damp heat test was performed on the multi crystalline Al-BSF sample according to IEC 61215-2:2016 international standard. The test sequence is 2 cycles of DH1000 exposure (1000 hours of exposure per cycle) followed by 3 cycles of DH400 exposure (400 hours of exposure per cycle). The final cumulative stress is DH3200 (total 3200 hours of DH exposure). The methodology for Raman measurement set up is similar to Chapter 5.2. The number of Raman spectra varies respective of the dimension of areal mapping and the magnification used. Two regions were scanned and analyzed – first, a crack propagating on the Si surface and second, the region with silver fingers.

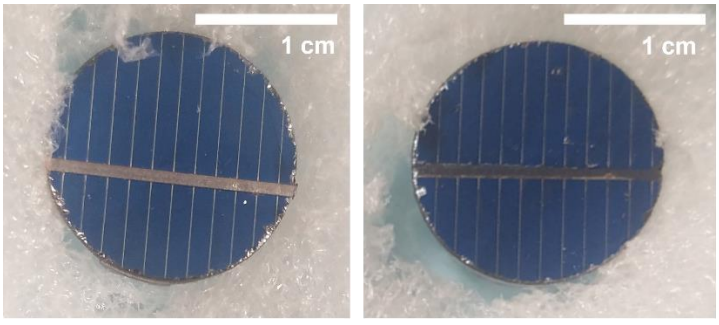

Figure 20: Fresh and damp heat tested cored out Al-BSF multicrystalline Si solar cell.

6.2 Raman characterization of Silicon surface

There are clear visual differences observed in the DH tested cell as compared to the control (untested cell). First, upon visual inspection the DH tested sample is slightly darker blue in color. An optical microscope-based examination also reveals a few micro-cracks on the surface of the DH tested sample. Raman microspectroscopy was used to understand the stress state of the Si around these cracks.

There are numerous reasons for the formation of cracks on the surface of a PV module. Micro-cracks in a PV system are caused by environmental conditions such as thermal cycling, humidity, cyclic pressure loads, wind loading, snowfall and hail. Such defects can cause inactive parts in the PV system that could lead to varying degrees of performance loss [65]. Micro-cracks in the cell, defects related to busbar contact, screen printed Ag finger and observation of inclusions on the surface of Si are the most common defects that can be detected with the help of EL, PL and LBIC [66-69].

We hypothesize that the extreme conditions of the damp heat testing i.e., thermal cycling is responsible for the formation of cracks in the DH tested cell [70]. Although the Raman signatures of the Si surface between the fresh and damp heat tested solar cell did not show any significant differences, the mechanical stress around the crack can be easily characterized. This is because, as stated in Chapter 3.2, the peak position of the Si TO phonon readily provides a measure of the stress state of Si. In particular -

$$\Delta\omega_3(cm^{-1}) = -4 \times 10^{-9} \left(\frac{\sigma_{xx} + \sigma_{yy}}{2}\right)(Pa) \qquad (5)$$

Thus, by monitoring the peak position of the Si around the crack, the stress state of the Si can be observed.

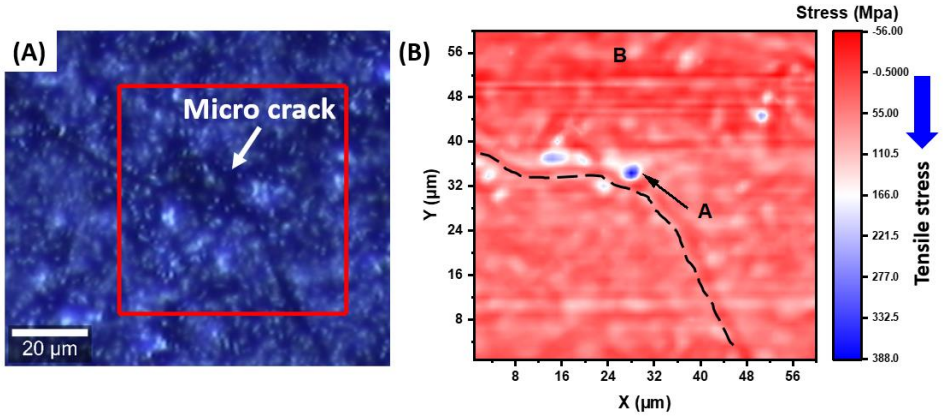

Figure 21: (A) Optical micrograph of a crack observed on the surface of the damp tested solar cell. (B) The map of the Raman peak position of Si provides a direct conversion to an equivalent stress map of the red boxed region.

Figure 21A shows the optical micrograph of the micro-crack taken under Raman microscope. The crack is clearly seen extending beyond the red boxed region. We measure the length of the crack to be ~ 125 µm with a maximum width of ~ 1.4 µm. It is interesting to note that the crack propagates from the bottom of the scanned region, but in the middle the crack slowly deflects towards the left at region marked 'A'.

To find the mechanical stress variation, an XY scan of the red boxed region was conducted. While it is possible to conduct a confocal measurement, here we will only focus on a planar XY mapping. The peak position information for the red boxed region is extracted using a custom-built MATLAB code and using the equation provided in the previous page. The respective stress map is plotted as shown in **Figure 21B**. The black dotted line indicates the crack on the stress map. The crack shows a minimal tensile stress of 0.5 MPa (corresponding to a minimum wave number of 520.49 cm^{-1}) whereas there is a localized region of high tensile stress corresponding to 388 MPa (a wavenumber of 519 cm^{-1}) along the crack front (marked as 'A' in Figure 21B). Further, the

region marked as ‘B’ is generally shown to develop a compressive stress with the maximum compression of -56 MPa (corresponding to a wavenumber shift to 520.7 cm^{-1}). Thus, the Raman mapping provides a comprehensive stress map in and around a crack as it propagates on the surface of a solar cell. It is also interesting to note that while the extent and magnitude of tensile stress is quite large, the compressive stress magnitude is relatively small and present in a well-defined region of the scanned area only.

Muhlstein proposed the term “reaction-layer fatigue” based on the investigation of growth of indentation induced cracks under cyclic loading in Si-based microelectromechanical systems (MEMS) in ambient air. A native Si oxide layer grows under the influence of local high stresses and laboratory humidity conditions. This Si dioxide is prone to stress corrosion cracking [71, 72]. As the cracks grow, new Si surface is revealed leading to further growth of the oxide layer. The crack in the native oxide layer penetrates the Si and grows across the specimen. We note that in the current DH3200 sample, the oxidation rate could be much severe, given that the testing environment is 85 % RH at 85 °C for 3200 h. This could influence the crack propagation along the surface of the Si wafer.

Danilewsky studied indentation induced crack propagation and fracture in Si wafer under thermal stress at 827 ^{o}C for 1500 seconds. Using *in situ* X-ray diffraction (XRD) it was observed that the strain accumulation occurs under thermal stress when a micro-crack is pinned. The pinning occurs because the strain energy associated with elastic region ahead of a crack tip is relatively low compared to the energy required for creating a fresh surface. [73].

In the case of the DH heat tested cell, we note that there is a 75 nm Si_3N_4 layer above the Si surface. Chemical vapor deposited (CVD) Si_3N_4, in general, are known to have built-in tensile

stresses [74, 75]. Diffusivity of moisture in Si_3N_4 layer is possible as is shown by Lee *et al* [76]. From the diffusivity values provided at 150 °C ($2x10^{-18}$ cm^2/sec) and activation energy (2.1 eV), we estimate the diffusivity of H_2O at 85 °C is 6.014×10^{-23} cm^2/s. For a 75 nm film the penetration time is therefore given to be

$$t = \frac{L^2}{D} = 1624\ hours \qquad (6)$$

This calculation shows that during the time of the test (3200 hours), water can penetrate the Si_3N_4 film and cause swelling.

Therefore, it is feasible that the moisture penetrates through the Si_3N_4 layer. This could lead to the swelling of the nitride to create stresses at the interface between Si_3N_4 and Si which would be tensile in nature. This fact is corroborated, in general, by observing that the crack shown in **Figure 21B** has tensile stresses adjacent to the crack. A region of compressive stress in region 'B' helps the crack to be slowly deflected towards the left.

6.3 Raman characterization of silver metallization

As expected, the Ag metallization undergoes oxidation as the solar cell is damp heat tested. However, we show that Raman micro-spectroscopy can clearly identify and map the oxide produced due to damp heat testing. Further, this oxide is chemically different from the oxide that results from the firing process, post-application of the Ag electrode paste.

Figure 22A shows the optical micrograph of silver metallization of a damp heat tested solar cell. The '+' marks show where single spot measurements were taken. The color labels red and blue, correspond to the colored Raman spectra in Figure 22B and Figure 22C, respectively.

In **Figure 22B**, the Raman spectra of the untested solar cell is also shown in black. It is clear from the graph that the 680 cm^{-1} peak of tested solar cell is sharp and has higher intensity compared to the broad 680 cm^{-1} of fresh solar cell. This indicates well-formed crystalline Ag_2O phase for the damp tested cell. Thus, the presence of moisture and low heat conditions can lead to crystallization of the Ag_2O phase.

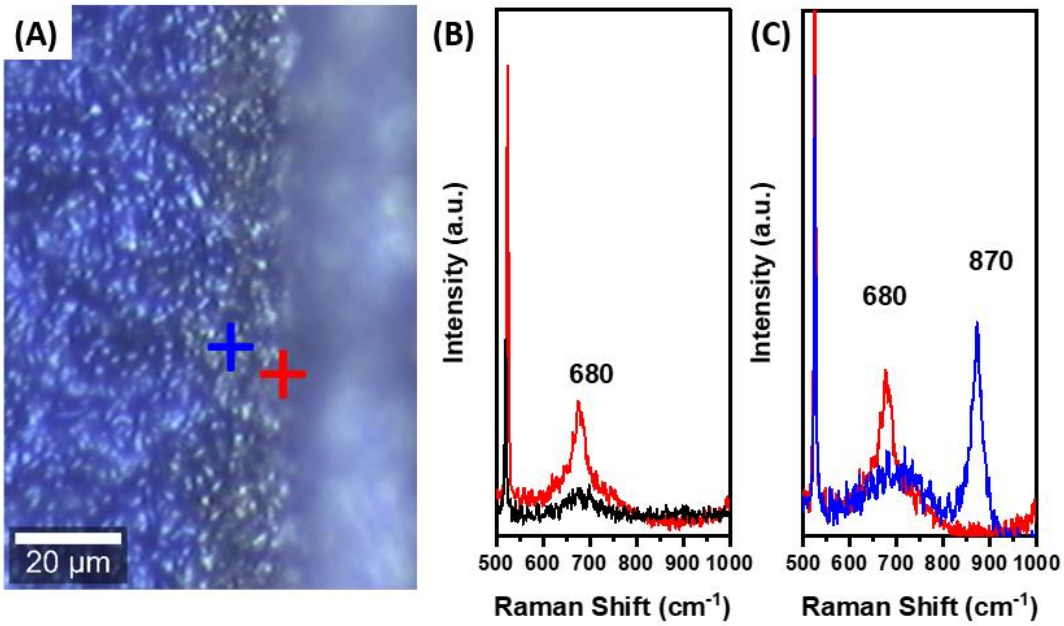

Figure 22: (A) Optical micrograph of a silver metallization of a damp heat tested solar cell. The '+' indicates the region of the acquired Raman spectrum (B) Raman spectrum comparison of a fresh and damp heat tested solar cell. The peak 680 cm^{-1} is sharp and intense compared to the unused cell. (C) Raman spectrum at the wall of silver metallization showing a sharp peak at 870 cm^{-1} indicating the presence of ν(Ag-O) bond.

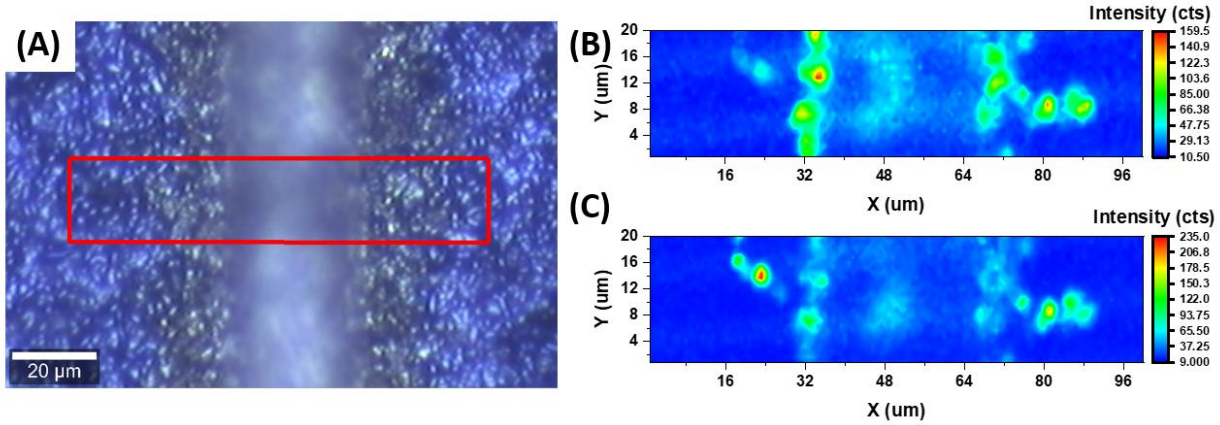

Figure 23: (A) Optical micrograph of the silver finger. The red boxed region indicates the areal mapping region (B) XY mapping of intensity of the silver oxide peak – 680 cm^{-1} (C) XY mapping of intensity of the silver oxide peak – 870 cm^{-1}.

In **Figure 22C**, the Raman spectra of the two '+' spots (red – close to the Ag finger; blue – away from the Ag finger) are compared. In addition to the 680 cm^{-1} band, a sharp peak at 870 cm^{-1} is also observed. This sharp peak can be attributed to the ν(Ag – O) bond of silver oxide and is not present on Ag fingers of untested solar cells [55].

Literature on silver – oxygen interaction suggests that silver is not oxidized by O_2 in ambient conditions [77, 78]. Only molecular or atomic oxygen is chemisorbed on the surface in three different atomic species: weakly chemisorbed surface atomic oxygen, atomic oxygen in subsurface and strongly chemisorbed surface atomic oxygen [77] [79].

Wiesinger *et al.*, have studied the influence of relative humidity on atmospheric silver corrosion [80]. Although the experimental conditions were not entirely comparable: RH of 0 %, 50 % and 90 % for 3 h, 6 h and 24 h at 22 °C, the study provides relevant insight into the corrosion mechanisms of silver. Their results showed that the RH favors the formation of 810 cm^{-1}, attributed to the Ag – O stretching vibration of the strongly chemisorbed surface oxygen. Certain Raman

bands were well developed as a function of RH % and time. The high intensity of the 810 cm^{-1} band could be attributed to two mechanisms:

1. Increased formation of oxide species on the surface

2. Effect of surface enhancement caused by the restructuring of surface due to the strong interaction of oxygen species [81, 82]

The peak at 870 cm^{-1} observed on the 'spill over' region and away from the Ag line could, therefore, be attributed to the strongly chemisorbed surface oxygen species as the conditions were RH 85 % at 85 °C for a total of 3200 h.

To understand the spatial distribution of the oxide phases on the Ag line, Raman area mapping was performed. **Figure 23A** shows the optical micrograph of the silver finger of a damp heat tested solar cell. A 100 x 20 μm^2 area was mapped under Raman microscope indicated by the red box. The XY intensity mapping of peak 680 cm^{-1} is shown in **Figure 23B**. **Figure 23C** shows the XY intensity mapping of peak 870 cm^{-1}. The peak 680 cm^{-1} is found to be present on the Ag line whereas the peak 870 cm^{-1} is seen over the 'spill over' regions. The sidewalls generate strong responses from both the 680 cm^{-1} and 870 cm^{-1} bands as the signal acquisition occurs parallel to the sidewall surface.

We observe that the intensity and distribution of the oxide phase on top of the Ag line is relatively low when compared to Figure 17C (untested sample). This is likely attributed to the shorter depth of focus of 20× magnification compared to 10× magnification used in the untested cell Ag metallization Raman areal mapping.

6.4 Conclusion

Raman microspectroscopy has been used to characterize a DH tested solar cell. Two regions – a crack propagating on the Si surface and the region with silver fingers were analyzed. First, it is proposed that the DH test caused moisture penetration through the ARC layer causing tensile stress in the nitride layer which may lead to initiation and propagation of the crack. Second, regions of compressive stress in the Si are shown to deflect cracks. Third, Raman on the DH tested cell Ag metallization is compared with tested solar cell. It is shown that the DH testing produces increased oxide species formation with a higher degree of crystallinity and stronger interaction with oxygen.

CHAPTER SEVEN: SYNCHRONOUS RAMAN MICROSCPECTROSCOPY AND LASER BEAM INDUCED CURRENT MEASUREMENTS OF A POLYCRYSTALLINE SILICON SOLAR CELL

We have established that Raman microspectroscopy is a powerful tool to characterize defects in a solar cell (Chapter 5) and is sensitive to material differences upon degradation (Chapter 6). In this chapter, we exploit the laser beam used to make the Raman measurements to concurrently perform LBIC measurements. The approach of Raman + LBIC can be broadly applied to the field of optoelectronic devices where structural, chemical and electrical results can be correlated in a "single shot" measurement modality.

7.1 Materials & Methodology

A polycrystalline Si solar cell with EVA encapsulation layer purchased from Aoshike Tech was used for Raman and LBIC measurements. Before performing any measurements, the EVA encapsulation layer was removed to avoid diffused scattering of the incident and reflected laser beam. Preliminary measurements confirm that the EVA layer is too thick. The solar cell was immersed in dichloromethane (anhydrous, 99.99%, contains 40 -150 ppm amylene as stabilizer) solution for 3 hours to dissolve the polymer layer. Raman spectroscopy before and after EVA removal confirmed that there is no residual EVA left on the Si surface.

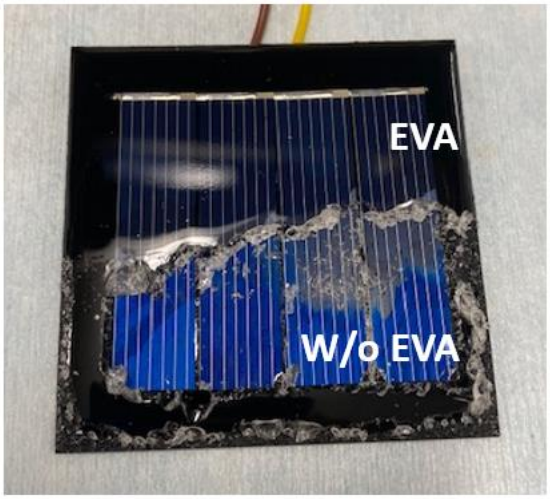

Figure 24: Polycrystalline Si solar panel showing part of the EVA polymer layer removed.

7.2 Instrumentation

The instrumentation details are provided in Chapter 4.

7.3 Raman and LBIC on Laser Induced Damage

To first understand the sensitivity differences and correlation between Raman and LBIC, controlled damage to the surface of a multicrystalline Si cell was induced by laser damage. A Tykma® MiniLase Laser Marking System with a 1064 nm laser is used to mark a 2 mm line on the Si surface as a function of laser power from 10 % to 100 %, where the maximum laser power is given as 15.91 mW/cm^2.

The control samples served as a 32 x 32 μm^2 control area, free of defects. This region was analyzed under Raman microscope while LBIC was synchronously recorded. **Figure 25A** shows the optical micrograph of the control area. **Figure 25B** shows the XY intensity mapping of Si. As observed in the multicrystalline Al-BSF solar cell presented in Chapter 5, the variation in Si

intensity mapping is reflective of the Si surface topology attributed to the texturing process. **Figure 25C** shows the XY LBIC mapping. It is interesting to see the texturing lines are recorded on the LBIC mapping as well. **Figure 25D** shows the distribution of photocurrent values. The current is a 'positively skewed' distribution. In these situations, the mode and range of the distribution are the best statistic for analysis. The mode is 1.01 µA. The photocurrent range (max – min = 1. 26 µA - 0.96 µA) is 0.30 µA. The positive skew indicates a mature technology for the solar cell where the majority of the photocurrent is limited at a minimum value of 1 µA or higher.

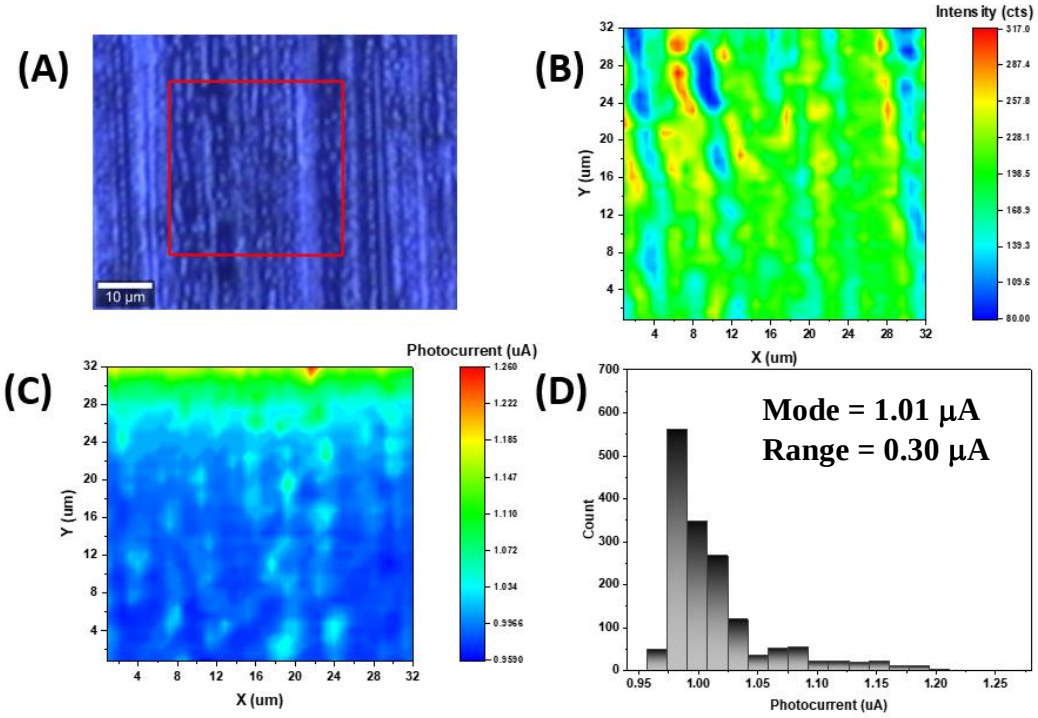

Figure 25: (A) Optical micrograph of a control area without any laser damage. The red boxed region indicates the Raman areal mapping (B) XY mapping of Si intensity (C) XY mapping of LBIC (D) Distribution of photocurrent values from the LBIC mapping inside the region.

Figure 26 shows the optical micrographs of laser induced damage on the Si surface as a function of power: (A) 10 % (B) 20% (C) 40% and (D) 60% (E) 80% (F) 100%. The visual

signature of the damage induced by 10% and 20% laser power is not readily observable on the Si surface as compared to the higher laser power. It is interesting to note that with increase in laser power, the edge of the damage line extends farther away from the intended damaged line.

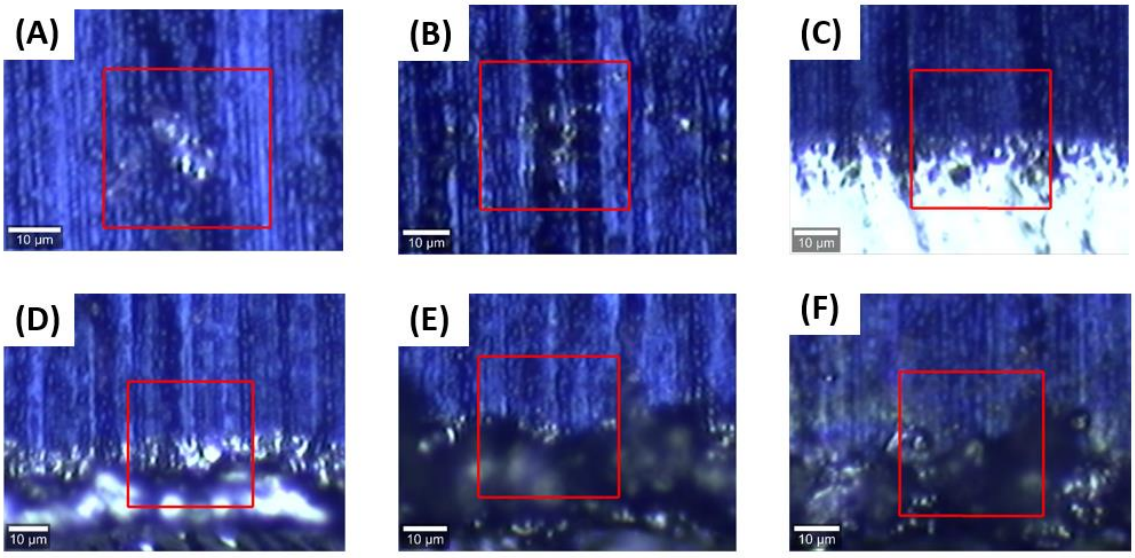

Figure 26: Optical micrograph of laser damaged Si surface with a laser power of (A) 10 % (B) 20 % (C) 40 % (D) 60 % (E) 80 % (F) 100 %.

Figure 27 shows the XY mappings of Raman Si intensity acquired from the laser damaged spots on the Si surface as a function of power: (A) 10 % (B) 20% (C) 40 % and (D) 60 % (E) 80 % (F) 100 %. The intensity mapping reflects not only the surface topology owing to the texturing process but also the laser damaged edges. The vertical lines running through the intensity mappings are attributed to the texturing process. The effect of plane of focus in regions away from the plane of focus (either above or below) cause lower peak intensities. The laser damaged spots of sample 40 %, 60 %, 80 % and 100 % show lower Raman intensities compared to the damage free Si surface and is overall very reflective of the optical micrographs.

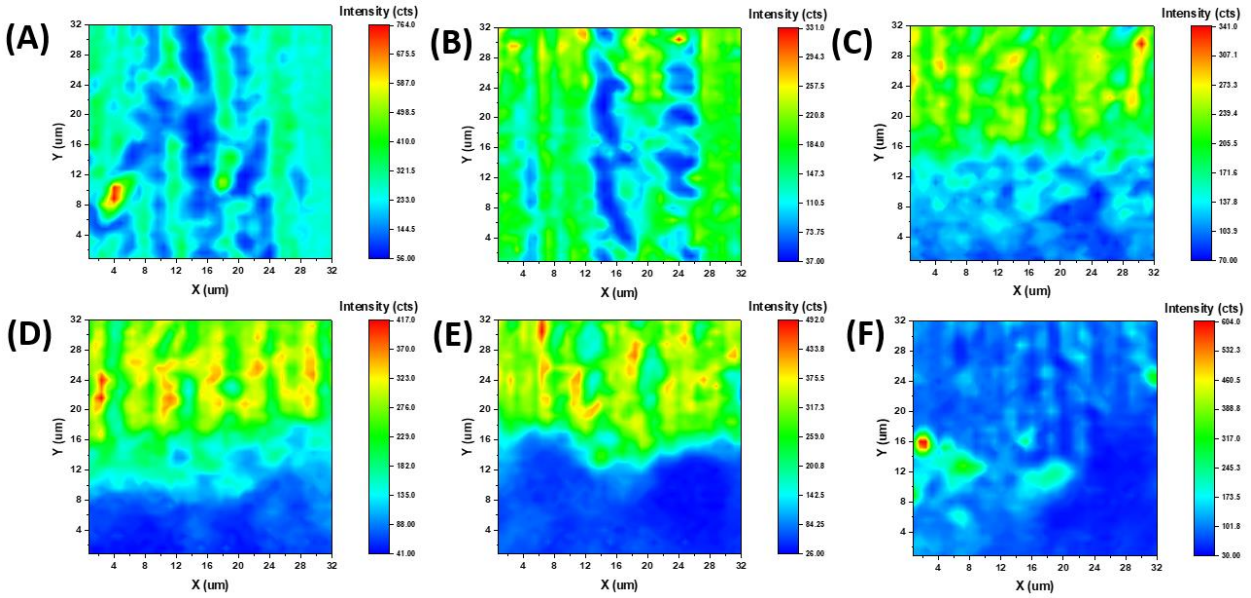

Figure 27: XY mappings of Raman Si intensity (A) 10 % (B) 20 % (C) 40 % (D) 60 % (E) 80 % (F) 100 %.

Figure 28 shows the LBIC XY mappings of the red boxed region shown in **Figure 26** respective to the laser power from 10 % to 100 %. As observed in **Figure 26C** control area, the texturing lines are recorded on the photocurrent mapping. Visually observing the LBIC indicates that major differences only show at 40% (6.36 mW/cm^2) and higher laser power. Under these higher laser power conditions, there is a distinct drop in LBIC corresponding to the damaged region in the microscope images of **Figure 26**.

The range of photocurrent values is calculated as a function of laser power and is provided as a table below along with other Raman and LBIC parameters. The control region range has a minimum difference of 0.3 µA compared to the laser damaged regions. This reveals that the LBIC measurements acquired via Raman microspectroscopy can identify performance loss points effectively.

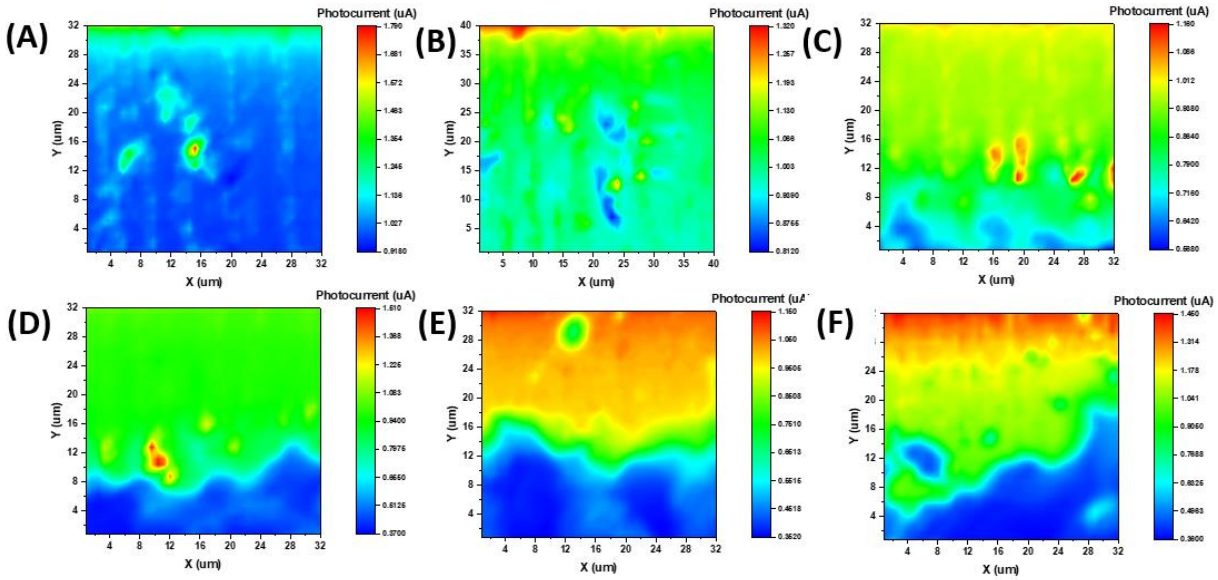

Figure 28: LBIC mappings of the red boxed region shown in Figure 25 (A) 10 % (B) 20 % (C) 40 % (D) 60 % (E) 80 % (F) 100 %.

Figure 29 shows the distribution of photocurrent values from LBIC mappings as a function of laser power. Compared with the control, the sample 10 % distribution is very similar and concentrated closer to 1 µA. With the increase in laser power from 10 % to 20 %, the distribution widens owing to the laser damage which is not very clear from the Raman intensity mapping. The photocurrent values for a 40 % laser damage have a wider distribution concentrated over the minimum current range i.e., left of 1 µA. For **Figure 29D**, **29E** and **29F**, we can see that the highest concentrated photocurrent value is ~ 1 µA. We also observe a bimodal distribution arising from the photocurrent values acquired over the damaged spots (bottom half of the mapping in all samples as seen in the optical micrographs). As we increase the laser power from 60 % to 80 %, we can clearly see that the lower photocurrent value concentration increases indicating that the performance loss is high in the 100 % sample.

Table 1: Raman and LBIC parameters as a function of laser power.

Laser power (%)	Power density (mW/cm^2)	Raman Si intensity range (cts)	LBIC range (µA)	LBIC mode (µA)
Control	-	237	0.3	1.01
10 %	1.59	708	0.88	1.01
20 %	3.18	294	0.52	1.02
40 %	6.36	271	0.6	0.958
60 %	9.54	376	1.13	1.01
80 %	12.73	466	0.8	1.01
100 %	15.91	574	1.09	1.1

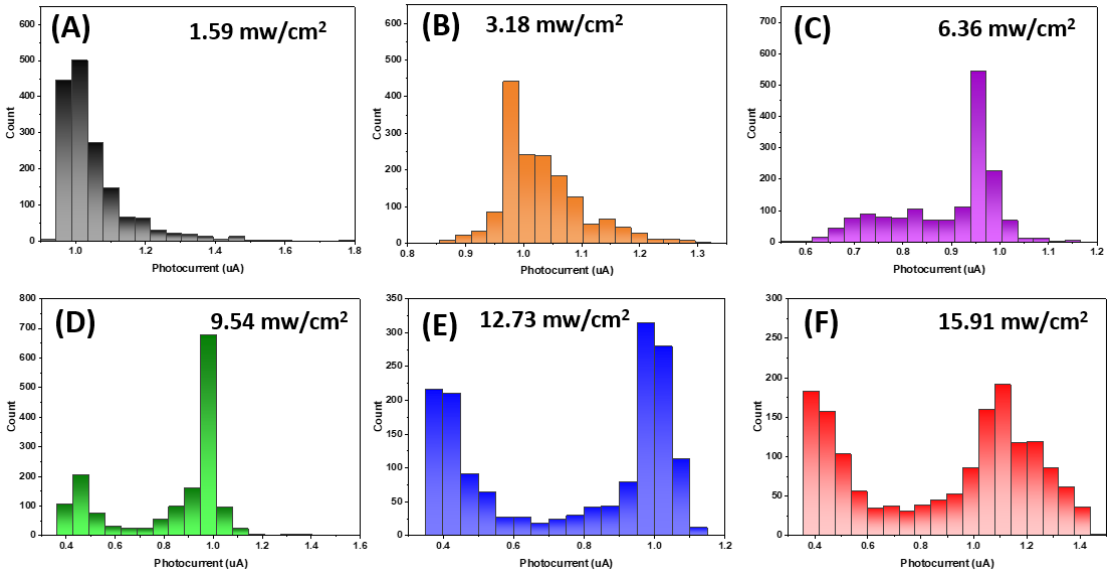

Figure 29: Distribution of photocurrent from the LBIC mappings shown in Figure 26 (A) 10 % (B) 20 % (C) 40 % (D) 60 % (E) 80 % (F) 100 %. In each graph, the extrema of the X scale correspond to the minimum and maximum values of the corresponding dataset.

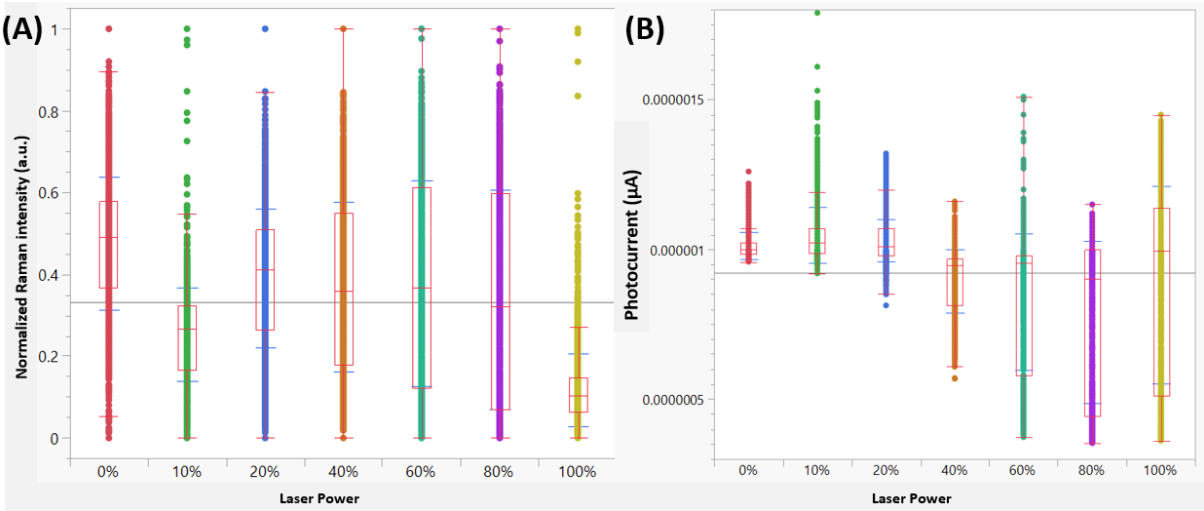

Figure 30: (A) Comparison of Si Raman intensity of laser induced damage spots as a function of power: 10% - 100% with control: 0% (B) Comparison of photocurrent of laser induced damage spots as a function of power: 10% - 100% with control: 0%.

Figure 30A shows the comparison of Si Raman intensity of laser induced damage spots as a function of laser power. **Figure 30B** shows the comparison LBIC of laser induced damage spots as a function of laser power. There is no definite trend observed from both Raman and LBIC ranges across different laser damaged spots. This is attributed to the selection of all datasets from the red boxed region which includes both damaged and undamaged Si regions.

From a much closer observation from **Figure 30B**, it appears that with the increase in laser power of the induced damage, there is a decrease in photocurrent. Observing the LBIC plot, major differences only show at 40% (6.36 mW/cm^2) and higher laser power as seen in LBIC mappings. This is only attributed to the performance loss points related to the damaged Si region. Although it is tempting to conclude that LBIC is more sensitive to solar cell degradation, more strenuous analysis is required to find the sensitivity of Raman and LBIC in characterizing solar cell degradation.

7.4 Raman and LBIC on other defects

Figure 31A shows the optical micrograph of a defect observed on the surface of solar cell. **Figure 31B** shows the XY intensity mapping of Si. The black dotted line marks the presence of the defect. As observed in the multicrystalline Al-BSF solar cell before, the variation in Si intensity mapping is reflective of the Si surface topology attributed to the texturing process. Along the line of the defect, the intensity drops to a minimum. This could be the effect of plane of focus as regions away from the plane (either above or below) cause lower peak intensities. **Figure 31C** shows the XY peak position mapping of Si. The peak position along the defect shifted to the higher wave number indicating that there are small amounts of crystal strain (compressive stress) along the defect.

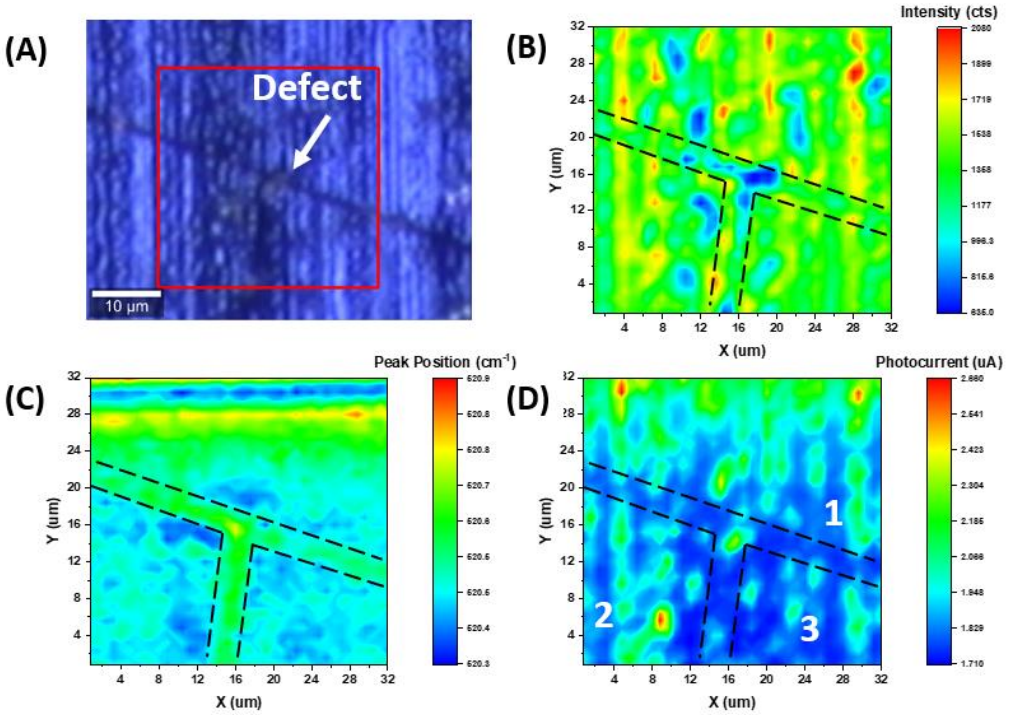

Figure 31: (A) Optical micrograph of a defect. The red boxed region indicates the Raman and LBIC areal mappings (B) XY mapping of intensity of Si (C) XY mapping of peak position of Si (D) XY mapping of photocurrent.

Figure 31D shows the XY photocurrent mapping of the defect region. The photocurrent is low at the defect compared to the entire map. Additionally, it is interesting to note that there are different regions associated with photocurrent: '1' with high photocurrent of the map, '2' with values less compared to 1 and '3' the lowest photocurrent. This result suggests that LBIC could be sensitive in detecting degradation in Si solar cell over Raman microspectroscopy measurement.

7.5 Raman and LBIC on Ag metallization

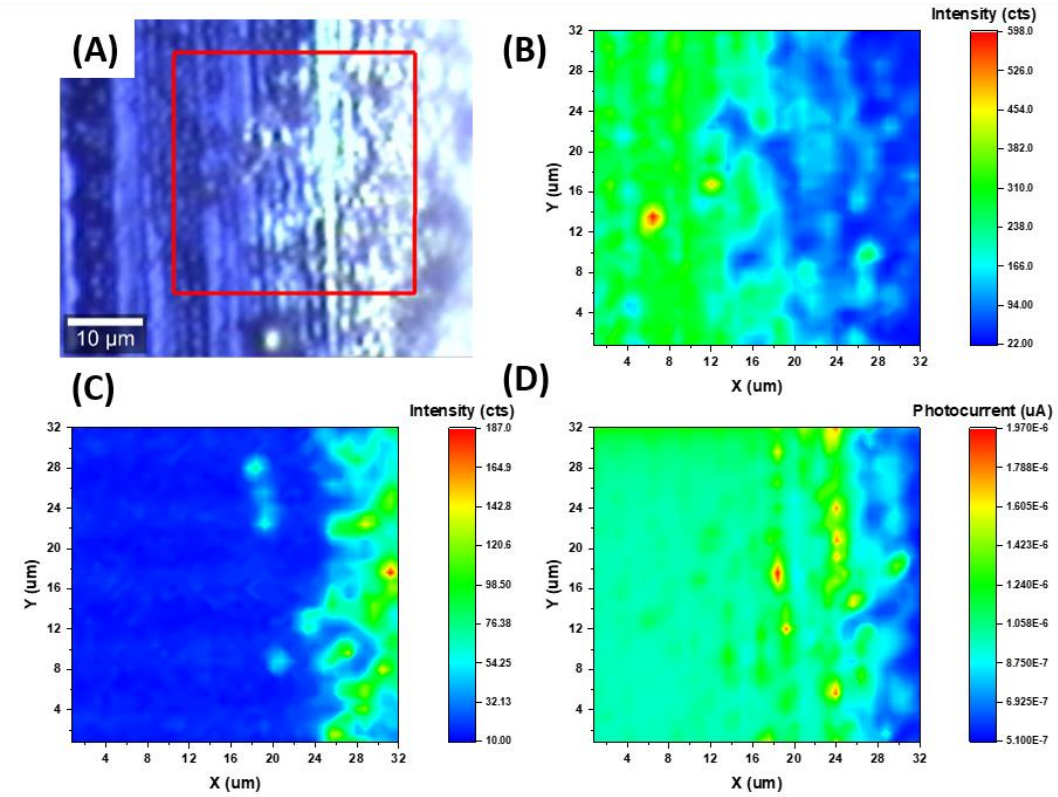

Figure 32: (A) Optical micrograph of silver finger. The red boxed region indicates the Raman and LBIC areal mappings (B) XY mapping of intensity of Si (C) XY mapping of intensity of silver oxide (D) XY mapping of photocurrent.

Figure 32A shows the optical micrograph of silver finger of the polycrystalline Si sample taken under Raman microscope. The XY intensity mapping of Si in **Figure 32B** and **32C**. The intensity of Si is maximum away from the finger and as the laser approaches the Ag line, the intensity decreases. On top of the Ag line, the Si peak disappears completely. Since the laser spot during the raster does not overlap with the previous spot, the information obtained at any given XY coordinate is expected to be free of neighboring site effects and thus, signal deconvolution is not needed.

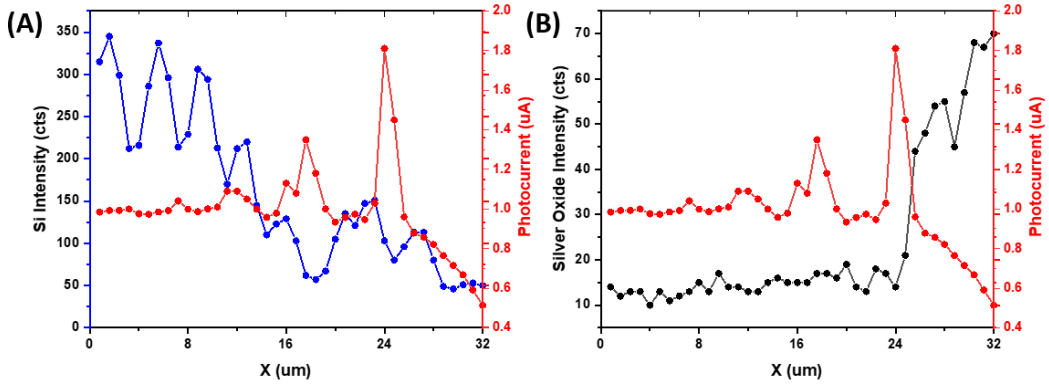

Figure 33: (A) Line scan comparison of Si intensity and LBIC (B) Line scan comparison of silver oxide intensity and LBIC.

The drop in intensity of Si can thus be attributed to compositional changes occurring at the site of interest. Figure 32C shows the XY intensity mapping of Ag_2O. This is in contrast with **Figure 32B** as the intensity of Ag_2O is zero away from the finger and maximum on the finger. **Figure 32D** shows the XY photocurrent mapping. At a very closer observation, this image is very reflective of Figure 32C but mirrored. The photocurrent is maximum away from the finger and once the laser is entirely on top of the Ag line, the photocurrent decreases to a minimum.

A horizontal line scan of the intensities of Si, Ag_2O and photocurrent taken along $Y = 20\ \mu m$ are compared to understand the correlation. **Figure 33A** shows the comparison of Si intensity

and photocurrent. The Si intensity gradually decreases along the line while the photocurrent is uniform away from the Ag line and reaches minimum on top of the Ag line. **Figure 33B** shows the comparison of Ag_2O intensity and photocurrent. The intensity of Ag_2O is zero and uniform away from the finger. The intensity increases while the photocurrent decreases at the Ag line. This is a very clear indication that the Ag_2O intensity (Ag line) and photocurrent are inversely correlated and the Pearson correlation coefficient for Si intensity and photocurrent: 0.1076 and Ag_2O intensity and photocurrent: -0.634 verifies the same.

7.6 Conclusion

In conclusion, Raman microspectroscopy has been successfully integrated with LBIC measurement modality. Three regions of interest: laser induced damage, a morphological defect and Ag metallization were characterized with the dual modality measurement. The results indicate that the μLBIC obtained via Raman microspectroscopy could be sensitive in characterizing the crystalline Si solar cell degradation compared to the Raman modality.

More analysis is required to understand the sensitivity of synchronous Raman and LBIC system in characterizing solar cell degradation and defects. In the future, comparison of localized regions within the Raman and LBIC mapping could reveal more information. For instance, in the laser damaged regions, the analysis shown in this work compares all the values from the red box. It would be interesting to compare Raman and LBIC values from the damaged spots alone excluding the undamaged Si area. Similarly, the three regions marked around the defect can be compared individually. This could reveal more information on the sensitivity of Raman and LBIC in characterizing Si solar cells.

A measurement of Raman and LBIC on a nano indented spot of Si solar cell surface could reveal the effectiveness of these individual modality in characterizing solar cell degradation. We have established that through Raman microspectroscopy, the stress around defects can be visualized. Additionally, the photocurrent around defects are significantly affected as we observed in chapter 7.4. Therefore, it would be interesting to study a controllably nano indented region with this modality. The sensitivity can be compared by visualizing how far the stress and photocurrent are affected from the spot on the solar cell surface due to degradation.

CHAPTER EIGHT: SUMMARY AND FUTURE PERSPECTIVES

8.1 Summary

In summary, the dissertation has explored the possibility of integrating Raman microspectroscopy with LBIC measurement modality to characterize solar cells. The utility of Raman microspectroscopy in obtaining insights into the surface and sub-surface quality of Si solar cells, defect detection and characterization has been successfully demonstrated. For the study, four prototypical regions were scanned and analyzed. Multi crystalline Si surface showed peak positions and FWHM comparable with a single crystalline Si wafer, indicating high crystalline quality of the textured Si solar cell surface; Regions with remnant saw marks were observed and, although a clear correlation between the image and Raman peaks were not observed, the peak and FWHM distributions were wider and at higher wavenumbers compared to regions on multi crystalline Si with no saw marks; Raman on Ag fingers indicated that ~ 200 nm thick Ag_2O could be detected up to 25 μm away from the line edges – a result of the screen-printing followed by firing process. An inclusion was characterized on the multi crystalline Si surface with the primary phase identified as nanocrystalline Si. The Si substrate around the inclusion was under tensile stress. Confocal mapping provided a non-destructive, 3D reconstruction of the inclusion, indicating the inclusion was embedded inside and protruded above the multi crystalline Si surface.

Raman microspectroscopy has been used to characterize a DH tested solar cell. Two regions – a crack propagating on the Si surface and the region with silver fingers were analyzed. It is proposed that the DH test caused moisture penetration through the ARC layer causing tensile stress which may lead to initiation and propagation of the crack; Regions of compressive stress in the Si are shown to deflect cracks. Additionally, Raman on the DH tested cell Ag metallization is

compared with untested solar cell. It is shown that the DH testing produces increased oxide species formation with a higher degree of crystallinity and stronger interaction with oxygen.

This work demonstrates that Raman microspectroscopy can be integrated with LBIC measurement modality to measure µLBIC. Three regions of interest: laser induced damage, defect and Ag metallization were characterized through the dual modality. The results indicate that the µLBIC obtained via Raman microspectroscopy seems sensitive in characterizing the crystalline Si solar cell compared to the Raman modality.

8.2 Future Perspectives

This dissertation successfully developed synchronous Raman and LBIC modality for solar cells. We demonstrated the use of the dual modality on crystalline Si solar cells.

The work suggests that LBIC seems sensitive in solar cell characterization compared to Raman microspectroscopy but there is no clear information based on the analysis performed. The lack of significant conclusion from the first approach of comparing the sensitivity of Raman and LBIC in characterizing solar cells suggests that more detailed analysis should be considered, as mentioned in chapter 7. In addition, we mainly focused on Raman intensity to reconstruct the chemical Raman maps here and compare with LBIC to characterize Si solar cells and understand the sensitivity of both systems in identifying degradation. However, Raman parameters such as peak position and FWHM should also be compared with LBIC in characterizing Si solar cells when using the modality. Such analysis could reveal more information than Raman intensity and LBIC.

This dual modality system can be explored for solar cell materials other than Si. Our remarks might change for a chemically rich system compared to a Si solar cell. Thus, optimizing the modality with different materials system (CdTe, ZnO, Perovskites) would help us understand the advantages and limitations across materials systems as well as characterization techniques.

The implementation of this technique would impact the solar cell production costs reducing $/watt. Manufacturing efficiency will be increased, and material loss will be reduced. A characterization technique with high sensitivity and spatial resolution in ambient operation will be developed thus enriching the solar cell manufacturing industry.

APPENDIX A: METHODOLOGY

The following content has been published in: J. P. Ganesan, N. Iqbal, M. Krsmanovic, F. Torres-Davila, A. Dickerson, K. O. Davis, L. Tetard and P. Banerjee, "Raman microspectroscopy of a multi-crystalline silicon solar cell", IEEE Journal of Photovoltaics, 2022.

It is important to verify that the laser power from the Raman microscope does not lead to temperature changes in the Si substrate. This is because an increase in temperature leads to a corresponding decrease in the TO phonon peak position of Si and thus, erroneous conclusions can be drawn [40]. We have studied the combined impact of laser power *and* temperature on the TO phonon peak position of single crystalline Si for the WITec® system. This is shown in **Appendix B**. Briefly, a single crystal, *p*-type (100) Si wafer was placed on a heated stage under the Raman microscope and the temperature was varied as 25 ^{o}C, 50 ^{o}C, 75 ^{o}C, 100 ^{o}C and 125 ^{o}C. At each temperature, the laser power was varied as, 4.4 mW, 13.5 mW, 24.3 mW and 32 mW. It was found that the temperature played a far critical role in lowering the TO phonon peak position wavenumber, from 520.3 cm^{-1} to 518 cm^{-1}. At any given temperature, increasing laser intensity did not result in a measurable shift in the TO phonon peak, indicating that the laser power did not cause any significant change in the temperature of the illuminated region of sample over and above the temperature of the substrate.

Optical images for profilometry were taken using a Keyence® Digital Microscope VHX-5000. The instrument used to perform *XY* micro-Raman spectroscopy was a WITec® 300 RA microscope. The mappings were performed using a laser excitation radiation of 532 nm. The penetration depth of this laser in Si is ~ 1.27 μm [83]. With the 20× objective used, the optical system provides a depth of focus (DOF) of 7 μm and a spot radius of 400 nm. The spot radius of

400 nm also provides the necessary information for conducting *XY* mapping. For example, an area of 25 × 25 μm^2 was mapped with a grid size of 31 × 31 (i.e., a total of 961 data points) with each step 800 nm apart which is equal to the spot diameter. The laser intensity used was 6 mW. Unless otherwise noted, the accumulation time was 1 second and every scan was integrated once. A larger area scan of 75 × 25 μm^2 with 2852 data points was performed with an objective of 20× on saw marks. The laser intensity used was 20 mW. For the Ag finger a lower magnification using a 10× objective was used, an area of 140 ×140 μm^2 was mapped with 2500 data points. The laser intensity used was 30 mW. For the inclusion, an objective of 10× was used on an area of 45 × 45 μm^2 mapped with 784 data points. The accumulation time was 2 seconds, and every scan was integrated once. The laser intensity used was 25 mW. Scan acquisition was conducted from 12 to 1200 cm^{-1} wavenumbers using a grating with 1800 gratings/mm and a resolution of 0.3 cm^{-1}. Total accumulation times for obtaining area scans ranged from tens of minutes to up to 3 hours long.

To achieve true confocal imaging of the inclusion reported in this work, a Horiba® LabRam Evolution system with a 785 nm laser was used. This laser wavelength allows for a penetration depth of 10 μm [83]. The experimental conditions for confocal mapping were 1 second integration time and 1 accumulation. A 50× long working distance (LWD) objective, 1800 gratings/mm and a laser intensity of 25 mW was used to conduct the 3D mapping. The total measurement time to collect all 36,938 spectra was 14 hours. Prior to conducting any Raman measurements, the equipment were calibrated using a pristine, single crystal Si wafer with the TO phonon adjusted to 520.5 cm^{-1}. Postprocessing of data including background subtraction and noise reduction through data averaging techniques were conducted with the instrument's proprietary software. Where necessary, data was exported as text files and custom-built MATLAB® codes

were written to extract the relevant information. These exceptions to data analyses will be described individually before the relevant results. As a clarification, Raman peak intensity maps imply mapping the height of the Raman peak.

APPENDIX B: SI RAMAN DEPENDECE OF TEMPATURE AND LASER POWER

The following content has been published in: J. P. Ganesan, N. Iqbal, M. Krsmanovic, F. Torres-Davila, A. Dickerson, K. O. Davis, L. Tetard and P. Banerjee, "Raman microspectroscopy of a multi-crystalline silicon solar cell", IEEE Journal of Photovoltaics, 2022.

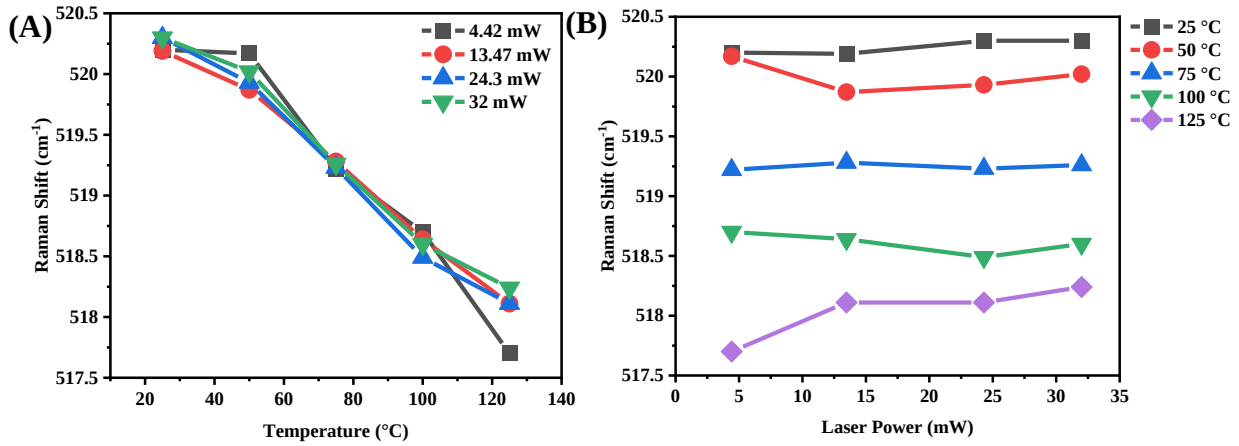

Figure 34: (A) The temperature dependence of the Si TO phonon peak position as a function of various laser powers. (B) The laser power dependence of the Si TO phonon peak position as a function of temperature.

To understand how laser heating may impact Raman peak position of Si, a single crystalline, p-type (100) prime Si wafer was placed on a heater stage under the WITec® 300 RA Raman microscope. It has been shown that increasing temperature leads to a drop in the TO phonon peak position of Si due to phonon 'softening'[40].

The heater stage temperature was raised from ambient (25 ^{o}C) to 125 ^{o}C at intervals of 25 ^{o}C. For thermal equilibration to set in, the sample was soaked at a given temperature for 5 minutes. The laser shutter was then opened, and the power varied as, 4.4, 13.5, 24.3 and 32 mW. The Si Raman peak was recorded at each laser power *and* wafer temperature. A strong dependence of the peak position on Si wafer temperature is observed in Figure 34A. In contrast, changing laser power

does not result in a change in the peak position as shown in Figure 34B. Thus, the laser beam does not lead to a significant change of temperature on the Si wafer surface.

APPENDIX C: SEM EDX OF A DEGRADED Al BSF CELL

The following figure has been published in: J. P. Ganesan, N. Iqbal, M. Krsmanovic, F. Torres-Davila, A. Dickerson, K. O. Davis, L. Tetard and P. Banerjee, "Raman microspectroscopy of a multi-crystalline silicon solar cell", IEEE Journal of Photovoltaics, 2022.

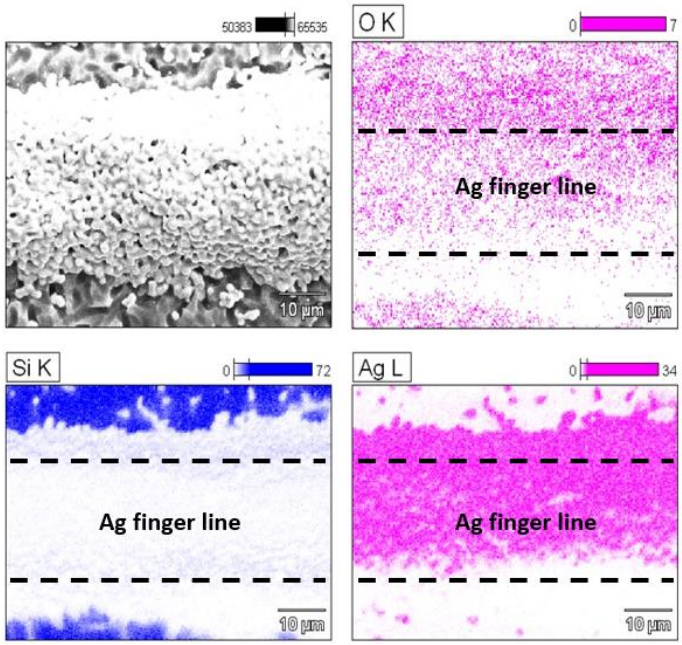

Figure 35: SEM EDX of O, Si and Ag across the silver line of a degraded multi crystalline Al-BSF solar cell module.

APPENDIX D: XPS DATA OF THE SILVER LINE OF A FRESH CELL

The following content has been published in: J. P. Ganesan, N. Iqbal, M. Krsmanovic, F. Torres-Davila, A. Dickerson, K. O. Davis, L. Tetard and P. Banerjee, "Raman microspectroscopy of a multi-crystalline silicon solar cell", IEEE Journal of Photovoltaics, 2022.

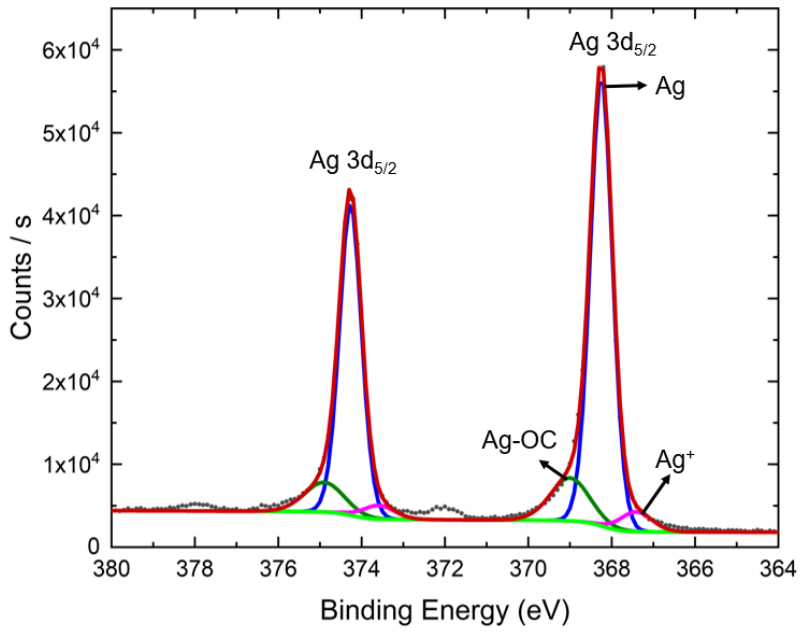

Figure 36: XPS data of the silver line of a fresh mono crystalline Al-BSF solar cell module.

Table 2: Atomic percent of Ag, Ag-O and Ag-OC detected on the silver line of a fresh mono crystalline Al-BSF solar cell module.

Binding Energy (eV)	**Peak**	**Atomic %**
368.25	Ag	82.51
367.4	Ag^{+} (Ag-O)	2.24
369	Ag-OC	15.26

APPENDIX E: POWER DEPENDENCE

The following figure has been published in: J. P. Ganesan, N. Iqbal, M. Krsmanovic, F. Torres-Davila, A. Dickerson, K. O. Davis, L. Tetard and P. Banerjee, "Raman microspectroscopy of a multi-crystalline silicon solar cell", IEEE Journal of Photovoltaics, 2022.

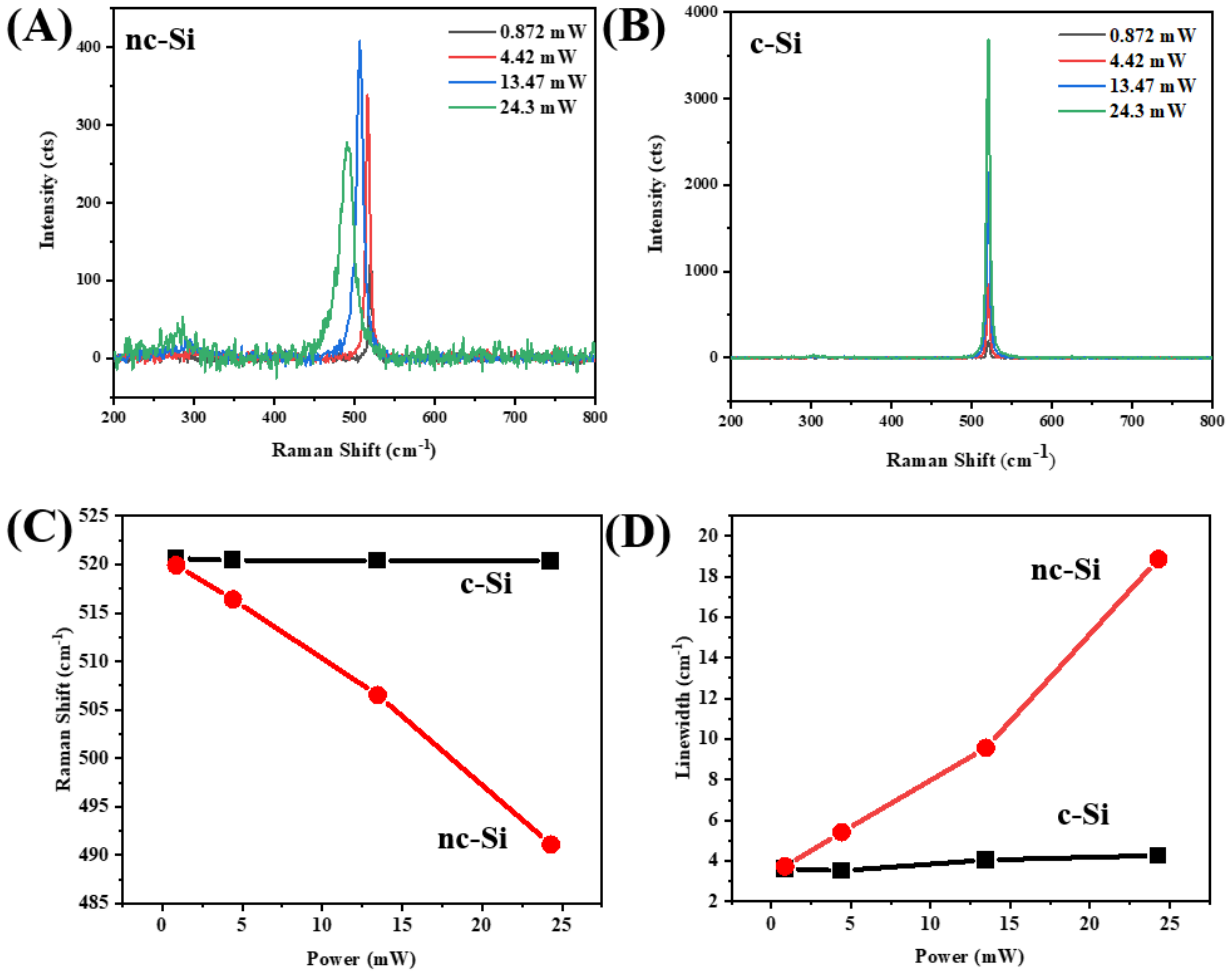

Figure 37: (A) Individual Raman spectra acquired on the inclusion (nanocrystalline Si i.e., nc-Si) with different laser power (B) Individual Raman spectra acquired on the multi crystalline Si (c-Si) with different laser power (C) Power dependence of peak shift for the Raman in multi crystalline Si (c-Si) and inclusion (nc-Si) (D) Power dependence of linewidth for the Raman in multi crystalline Si (c-Si) and inclusion (nc-Si).

APPENDIX F: POWER CONVERSION EFFICIENCY MEASUREMENT

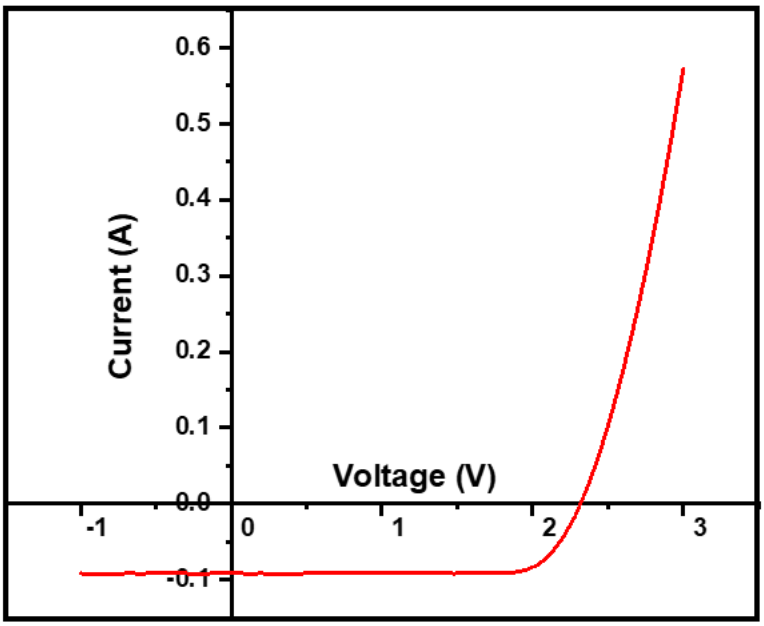

Figure 38: *I-V* characteristics of the polycrystalline Si solar cell.

To calculate the power conversion efficiency, the *IV* characteristics of the polycrystalline Si solar cell is studied over a voltage range of -1 V to +3 V. A Keithley source meter controlled by the I-V software was used to perform the *I-V* study. An incident power of 100 mW/cm^2 was used. The power conversion efficiency was 11.52 % with a fill factor of 80.6 %. The open-circuit voltage V_{oc} was calculated to be 2.31 V.

APPENDIX G: COPYRIGHT PERMISSION

Chapter 5

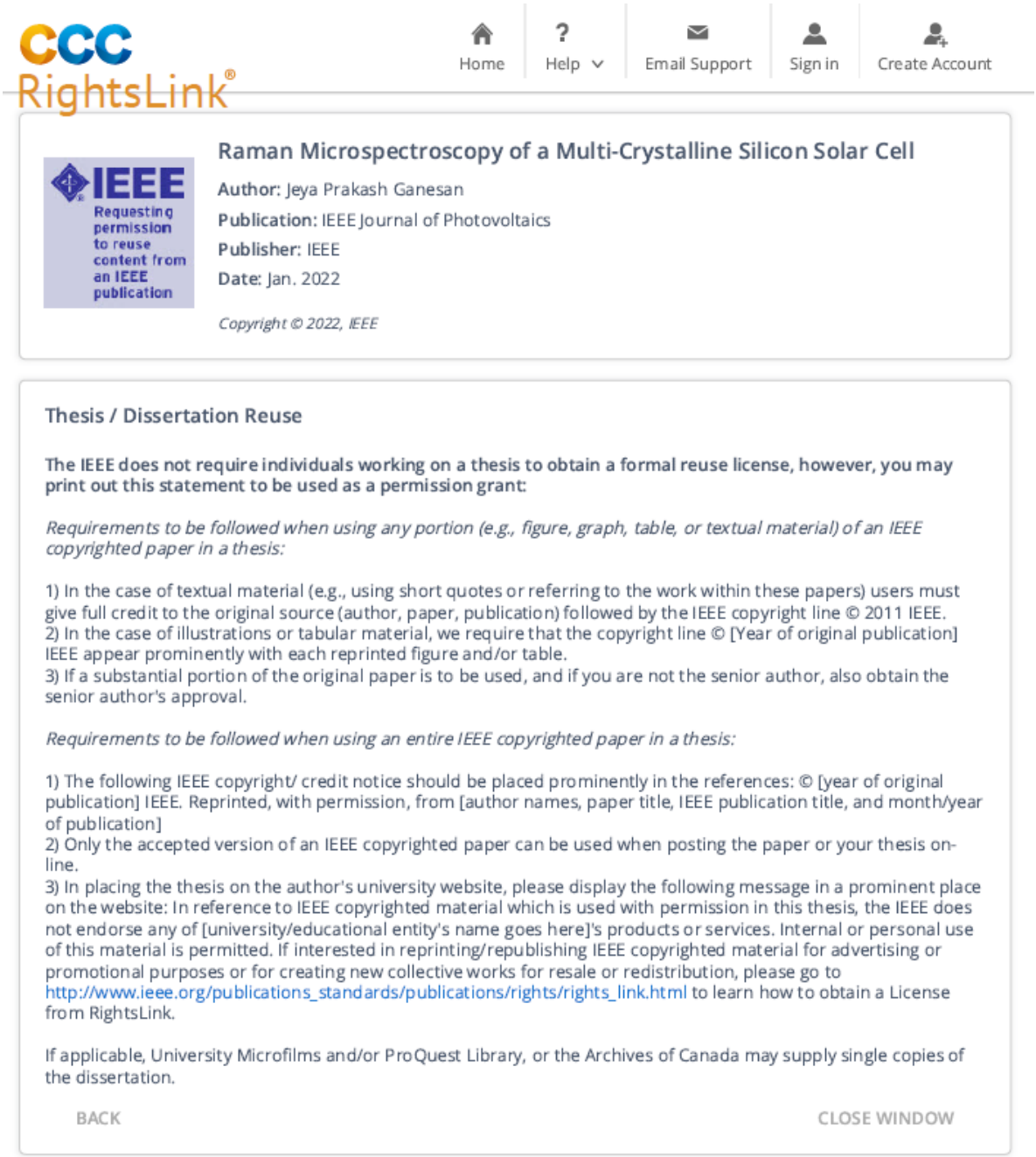

CCC RightsLink®

Home | Help | Email Support | Sign in | Create Account

IEEE Requesting permission to reuse content from an IEEE publication

Raman Microspectroscopy of a Multi-Crystalline Silicon Solar Cell

Author: Jeya Prakash Ganesan

Publication: IEEE Journal of Photovoltaics

Publisher: IEEE

Date: Jan. 2022

Copyright © 2022, IEEE

Thesis / Dissertation Reuse

The IEEE does not require individuals working on a thesis to obtain a formal reuse license, however, you may print out this statement to be used as a permission grant:

Requirements to be followed when using any portion (e.g., figure, graph, table, or textual material) of an IEEE copyrighted paper in a thesis:

1) In the case of textual material (e.g., using short quotes or referring to the work within these papers) users must give full credit to the original source (author, paper, publication) followed by the IEEE copyright line © 2011 IEEE.
2) In the case of illustrations or tabular material, we require that the copyright line © [Year of original publication] IEEE appear prominently with each reprinted figure and/or table.
3) If a substantial portion of the original paper is to be used, and if you are not the senior author, also obtain the senior author's approval.

Requirements to be followed when using an entire IEEE copyrighted paper in a thesis:

1) The following IEEE copyright/ credit notice should be placed prominently in the references: © [year of original publication] IEEE. Reprinted, with permission, from [author names, paper title, IEEE publication title, and month/year of publication]
2) Only the accepted version of an IEEE copyrighted paper can be used when posting the paper or your thesis on-line.
3) In placing the thesis on the author's university website, please display the following message in a prominent place on the website: In reference to IEEE copyrighted material which is used with permission in this thesis, the IEEE does not endorse any of [university/educational entity's name goes here]'s products or services. Internal or personal use of this material is permitted. If interested in reprinting/republishing IEEE copyrighted material for advertising or promotional purposes or for creating new collective works for resale or redistribution, please go to http://www.ieee.org/publications_standards/publications/rights/rights_link.html to learn how to obtain a License from RightsLink.

If applicable, University Microfilms and/or ProQuest Library, or the Archives of Canada may supply single copies of the dissertation.

BACK CLOSE WINDOW

LIST OF REFERENCES

[1] M. A. Green, E. D. Dunlop, J. Hohl-Ebinger, M. Yoshita, N. Kopidakis, and X. Hao, "Solar cell efficiency tables (version 56)," *Progress in Photovoltaics: Research and Applications,* vol. 28, no. 7, pp. 629-638, 2020, doi: 10.1002/pip.3303.

[2] K. Yamamoto, K. Yoshikawa, H. Uzu, and D. Adachi, "High-efficiency heterojunction crystalline Si solar cells," *Jpn. J. Appl. Phys.,* vol. 57, no. 8S3, p. 08RB20, 2018, doi: 10.7567/jjap.57.08rb20.

[3] D. Quansah, M. Adaramola, G. Takyi, and I. Edwin, "Reliability and Degradation of Solar PV Modules—Case Study of 19-Year-Old Polycrystalline Modules in Ghana," *Technologies,* vol. 5, no. 2, 2017, doi: 10.3390/technologies5020022.

[4] "Annual Energy Outlook 2020, U.S. Energy Information Administration (EIA), Office of Energy Analysis, U.S. Department of Energy." [Online]. Available: https://www.eia.gov/aeo

[5] L. C. Andreani, A. Bozzola, P. Kowalczewski, M. Liscidini, and L. Redorici, "Silicon solar cells: toward the efficiency limits," *Advances in Physics: X,* vol. 4, no. 1, p. 1548305, 2019, doi: 10.1080/23746149.2018.1548305.

[6] R. W. Miles, "Photovoltaic solar cells: Choice of materials and production methods," vol. 80, no. 10, pp. 1090-1097, 2006, doi: 10.1016/j.vacuum.2006.01.006.

[7] W. Durisch, J. Urban, and G. Smestad, "Characterisation of solar cells and modules under actual operating conditions," *Renewable Energy,* vol. 8, no. 1-4, pp. 359-366, 1996, doi: 10.1016/0960-1481(96)88878-1.

[8] K. O. Davis *et al.*, "Manufacturing metrology for c-Si module reliability and durability Part II: Cell manufacturing," *Renewable and Sustainable Energy Reviews,* vol. 59, pp. 225-252, 2016, doi: 10.1016/j.rser.2015.12.217.

[9] E. J. Schneller *et al.*, "Manufacturing metrology for c-Si module reliability and durability Part III: Module manufacturing," *Renewable and Sustainable Energy Reviews,* vol. 59, pp. 992-1016, 2016, doi: 10.1016/j.rser.2015.12.215.

[10] H. Seigneur *et al.*, "Manufacturing metrology for c-Si photovoltaic module reliability and durability, Part I: Feedstock, crystallization and wafering," *Renewable and Sustainable Energy Reviews,* vol. 59, pp. 84-106, 2016, doi: 10.1016/j.rser.2015.12.343.

[11] Q. Chen and Y. Zhang, "The reversal of the laser-beam-induced-current contrast with varying illumination density in a Cu2ZnSnSe4 thin-film solar cell," *Appl. Phys. Lett.*, vol. 103, no. 24, p. 242104, 2013, doi: 10.1063/1.4844815.

[12] O. Breitenstein, J. Bauer, and J. P. Rakotoniaina, "Material-induced shunts in multicrystalline silicon solar cells," *Semic,* vol. 41, no. 4, pp. 440-443, 2007, doi: 10.1134/s106378260704015x.

[13] S. G. Susanne Richter, Tabea Luka, Marko Turek, Martina Werner, and C. Hagendorf, "Microscopic Light-Beam Induced Current Measurement for High-Resolution Solar Cell Characterization," 2016.

[14] "NREL." https://www.nrel.gov/ (accessed.

[15] "PV Education." https://www.pveducation.org/ (accessed.

[16] K. Sopian, S. L. Cheow, and S. H. Zaidi, "An overview of crystalline silicon solar cell technology: Past, present, and future," 2017.

[17] D. B. Khadka, Y. Shirai, M. Yanagida, and K. Miyano, "Tailoring the Film Morphology and Interface Band Offset of Caesium Bismuth Iodide based Pb Free Perovskite Solar Cells," *Journal of Materials Chemistry C,* 2019.

[18] M. Kong *et al.*, "Nontoxic (CH3NH3)3Bi2I9 perovskite solar cells free of hole conductors with an alternative architectural design and a solution-processable approach," *RSC Advances,* vol. 7, no. 56, pp. 35549-35557, 2017, doi: 10.1039/c7ra04924b.

[19] Z. Zhang *et al.*, "High-Quality (CH3NH3)3Bi2I9 Film-Based Solar Cells: Pushing Efficiency up to 1.64," *J. Phys. Chem. Lett.,* vol. 8, no. 17, pp. 4300-4307, Sep 7 2017, doi: 10.1021/acs.jpclett.7b01952.

[20] P. V. Kamat, "Evolution of Perovskite Photovoltaics and Decrease in Energy Payback Time," *The Journal of Physical Chemistry Letters,* vol. 4, no. 21, pp. 3733-3734, 2013, doi: 10.1021/jz402141s.

[21] Z. Liu *et al.*, "Anti-solvent spin-coating for improving morphology of lead-free (CH3NH3)3Bi2I9 perovskite films," *SN Applied Sciences,* vol. 1, no. 7, 2019, doi: 10.1007/s42452-019-0727-6.

[22] S. S. Shin *et al.*, "Solvent-Engineering Method to Deposit Compact Bismuth-Based Thin Films: Mechanism and Application to Photovoltaics," *Chem. Mater.,* vol. 30, no. 2, pp. 336-343, 2018, doi: 10.1021/acs.chemmater.7b03227.

[23] C. Moura, R. Tare, R. Oreffo, and S. Mahajan, "Raman spectroscopy and coherent anti-Stokes Raman scattering imaging: Prospective tools for monitoring skeletal cells and skeletal regeneration," *Journal of The Royal Society Interface,* vol. 13, p. 20160182, 05/11 2016, doi: 10.1098/rsif.2016.0182.

[24] C. V. Raman and K. S. Krishnan, "A New Type of Secondary Radiation," *Nature*, vol. 121, no. 3048, pp. 501-502, 1928/03/01 1928, doi: 10.1038/121501c0.

[25] R. L. McCreery, *Raman spectroscopy for chemical analysis* (A series of monographs on analytical chemistry and its applications). John Wiley & Sons, Inc., , 2000.

[26] E. Instruments. "Raman Spectroscopy." https://www.edinst.com/blog/what-is-raman-spectroscopy/ (accessed.

[27] J. H. Parker, D. W. Feldman, and M. Ashkin, "Raman Scattering by Silicon and Germanium," *Phys. Rev.*, vol. 155, no. 3, pp. 712-714, 1967, doi: 10.1103/PhysRev.155.712.

[28] G. Kolb, T. Salbert, and G. Abstreiter, "Raman-microprobe study of stress and crystal orientation in laser-crystallized silicon," *J. Appl. Phys.*, vol. 69, no. 5, pp. 3387-3389, 1991, doi: 10.1063/1.348516.

[29] T. C. Damen, S. P. S. Porto, and B. Tell, "Raman Effect in Zinc Oxide," *Phys. Rev.*, vol. 142, no. 2, pp. 570-574, 1966, doi: 10.1103/PhysRev.142.570.

[30] D. Caffrey *et al.*, "Crystallographic Characterisation of Ultra-Thin, or Amorphous Transparent Conducting Oxides—The Case for Raman Spectroscopy," *Materials*, vol. 13, no. 2, p. 267, 2020, doi: 10.3390/ma13020267.

[31] K. Fleischer *et al.*, "Raman spectra of p-type transparent semiconducting Cr2O3:Mg," *Thin Solid Films*, vol. 594, pp. 245-249, 2015, doi: 10.1016/j.tsf.2015.03.076.

[32] O. Hollricher and W. Ibach, "High-Resolution Optical and Confocal Microscopy," Springer Berlin Heidelberg, 2010, pp. 1-20.

[33] Xi *et al.*, "Micro-Raman Study of Thermal Transformations of Sulfide and Oxysalt Minerals Based on the Heat Induced by Laser," *Minerals,* vol. 9, p. 751, 12/03 2019, doi: 10.3390/min9120751.

[34] B. Li, D. Yu, and S.-L. Zhang, "Raman spectral study of silicon nanowires," *PhRvB,* vol. 59, no. 3, pp. 1645-1648, 1999, doi: 10.1103/physrevb.59.1645.

[35] D. Beeman, R. Tsu, and M. F. Thorpe, "Structural information from the Raman spectrum of amorphous silicon," vol. 32, no. 2, pp. 874-878, 1985, doi: 10.1103/physrevb.32.874.

[36] E. C. Honea *et al.*, "Raman spectra of size-selected silicon clusters and comparison with calculated structures," vol. 366, no. 6450, pp. 42-44, 1993, doi: 10.1038/366042a0.

[37] P. Yogi *et al.*, "Quantifying the Short-Range Order in Amorphous Silicon by Raman Scattering," *Anal. Chem.,* 2018, doi: 10.1021/acs.analchem.8b01352.

[38] D. Tuschel, "Stress, Strain, and Raman Spectroscopy," *Spectroscopy,* vol. 34, no. 9, pp. 10-21, 2019.

[39] T. Nikitin, S. Novikov, and L. Khriachtchev, "Giant Raman gain in annealed silicon-rich silicon oxide films: Measurements at 785 nm," *Appl. Phys. Lett.,* vol. 103, no. 15, 2013, doi: 10.1063/1.4824732.

[40] S. Périchon, V. Lysenko, B. Remaki, D. Barbier, and B. Champagnon, "Measurement of porous silicon thermal conductivity by micro-Raman scattering," *J. Appl. Phys.,* vol. 86, no. 8, pp. 4700-4702, 1999, doi: 10.1063/1.371424.

[41] I. De Wolf, H. E. Maes, and S. K. Jones, "Stress measurements in silicon devices through Raman spectroscopy: Bridging the gap between theory and experiment," *J. Appl. Phys.,* vol. 79, no. 9, pp. 7148-7156, 1996, doi: 10.1063/1.361485.

[42] Z. Su *et al.*, "Temperature-Dependent Raman Scattering of Silicon Nanowires," *The Journal of Physical Chemistry B,* vol. 110, no. 3, pp. 1229-1234, 2006, doi: 10.1021/jp055869o.

[43] V. T. Srikar, A. K. Swan, M. S. Unlu, B. B. Goldberg, and S. M. Spearing, "Micro-Raman measurement of bending stresses in micromachined silicon flexures," vol. 12, no. 6, pp. 779-787, 2003, doi: 10.1109/jmems.2003.820280.

[44] M. Becker, U. GöSele, A. Hofmann, and S. Christiansen, "Highly p-doped regions in silicon solar cells quantitatively analyzed by small angle beveling and micro-Raman spectroscopy," vol. 106, no. 7, p. 074515, 2009, doi: 10.1063/1.3236571.

[45] C. Droz, E. Vallat-Sauvain, J. Bailat, L. Feitknecht, J. Meier, and A. Shah, "Relationship between Raman crystallinity and open-circuit voltage in microcrystalline silicon solar cells," *Sol. Energy Mater. Sol. Cells,* vol. 81, no. 1, pp. 61-71, 2004, doi: 10.1016/j.solmat.2003.07.004.

[46] M. Israil, S. A. Anwar, and M. Z. Abdullah, "Automatic detection of micro-crack in solar wafers and cells: a review," vol. 35, no. 5, pp. 606-618, 2013, doi: 10.1177/0142331212457583.

[47] F. J. Vorster and E. E. Van Dyk, "High saturation solar light beam induced current scanning of solar cells," *Rev. Sci. Instrum.,* vol. 78, no. 1, p. 013904, 2007, doi: 10.1063/1.2432408.

[48] J. I. Marek, "Light-beam-induced current characterization of grain boundaries," vol. 55, no. 2, p. 318, 1984, doi: 10.1063/1.333047.

[49] M. B. Rabha, W. Dimassi, M. Bouaïcha, H. Ezzaouia, and B. Bessais, "Laser-beam-induced current mapping evaluation of porous silicon-based passivation in polycrystalline silicon solar cells," vol. 83, no. 5, pp. 721-725, 2009, doi: 10.1016/j.solener.2008.11.002.

[50] C. A. Musca, D. A. Redfern, J. M. Dell, and L. Faraone, "Laser beam induced current as a tool for HgCdTe photodiode characterisation," vol. 31, no. 7, pp. 537-544, 2000, doi: 10.1016/s0026-2692(00)00027-6.

[51] C. A. Musca, D. A. Redfern, E. P. G. Smith, J. M. Dell, L. Faraone, and J. Bajaj, "Junction depth measurement in HgCdTe using laser beam induced current (LBIC)," *JEMat*, vol. 28, no. 6, pp. 603-610, 1999, doi: 10.1007/s11664-999-0042-x.

[52] S. C. W. Zhaoning Song, Brandon L. Tompkins, Geethika K. Liyanage, Adam B. Philips, Randy J. Ellingson and Michael J. Heben, "Spatially Resolved Characterization of Solution Processed Perovskite Solar Cells Using the LBIC Technique," presented at the IEEE. [Online]. Available: https://dx.doi.org/10.1109/pvsc.2015.7355676.

[53] F. J. Navas, R. AlcáNtara, C. FernáNdez-Lorenzo, and J. N. MartíN, "A methodology for improving laser beam induced current images of dye sensitized solar cells," vol. 80, no. 6, p. 063102, 2009, doi: 10.1063/1.3147381.

[54] S. Banerjee *et al.*, "Phase and stress evolution of Si swarf in the diamond-coated wire sawing of Si ingots," *Int. J. Adv. Manuf. Technol.*, vol. 89, no. 1-4, pp. 735-742, 2016, doi: 10.1007/s00170-016-9102-6.

[55] C.-B. Wang, G. Deo, and I. E. Wachs, "Interaction of Polycrystalline Silver with Oxygen, Water, Carbon Dioxide, Ethylene, and Methanol: In Situ Raman and Catalytic Studies,"

The Journal of Physical Chemistry B, vol. 103, no. 27, pp. 5645-5656, 1999, doi: 10.1021/jp984363l.

[56] S. Wu *et al.*, "Investigation of the mechanism of the Ag/SiNx firing-through process of screen-printed silicon solar cells," vol. 4, no. 46, p. 24384, 2014, doi: 10.1039/c4ra00072b.

[57] T. Matsuda, K. Inami, K. Motoyama, T. Sano, and A. Hirose, "Silver oxide decomposition mediated direct bonding of silicon-based materials," *Sci. Rep.*, vol. 8, no. 1, p. 10472, 2018/07/11 2018, doi: 10.1038/s41598-018-28788-x.

[58] A. J. Varkey and A. F. Fort, "Some optical properties of silver peroxide (AgO) and silver oxide (Ag2O) films produced by chemical-bath deposition," *Solar Energy Materials and Solar Cells*, vol. 29, no. 3, pp. 253-259, 1993/04/01/ 1993, doi: https://doi.org/10.1016/0927-0248(93)90040-A.

[59] S. Banerjee, A. K. Maity, and D. Chakravorty, "Quantum confinement effect in heat treated silver oxide nanoparticles," *Journal of Applied Physics*, vol. 87, no. 12, pp. 8541-8544, 2000, doi: 10.1063/1.373575.

[60] M. S. G. Mohammed, E. Cazzanelli, A. Fasanella, and M. Castriota, "Silicon Nanocrystals on the Surface of Standard Si Wafers: A Micro-Raman Investigation," *Journal of Materials Science and Chemical Engineering*, vol. 06, no. 07, pp. 104-116, 2018, doi: 10.4236/msce.2018.67012.

[61] Z. Sui, P. P. Leong, I. P. Herman, G. S. Higashi, and H. Temkin, "Raman analysis of light-emitting porous silicon," *Appl. Phys. Lett.*, vol. 60, no. 17, pp. 2086-2088, 1992, doi: 10.1063/1.107097.

[62] J. Yang, S. Banerjee, J. Wu, Y. Myung, O. Rezvanian, and P. Banerjee, "Phase and stress evolution in diamond microparticles during diamond-coated wire sawing of Si ingots," *The International Journal of Advanced Manufacturing Technology,* vol. 82, no. 9-12, pp. 1675-1682, 2015, doi: 10.1007/s00170-015-7446-y.

[63] L. Yang and A. J. Minnich, "Thermal transport in nanocrystalline Si and SiGe by ab initio based Monte Carlo simulation," *Sci. Rep.,* vol. 7, p. 44254, Mar 14 2017, doi: 10.1038/srep44254.

[64] Z. Wang, J. E. Alaniz, W. Jang, J. E. Garay, and C. Dames, "Thermal conductivity of nanocrystalline silicon: importance of grain size and frequency-dependent mean free paths," *Nano Lett.,* vol. 11, no. 6, pp. 2206-13, Jun 8 2011, doi: 10.1021/nl1045395.

[65] E. Andenæs, B. P. Jelle, K. Ramlo, T. Kolås, J. Selj, and S. E. Foss, "The influence of snow and ice coverage on the energy generation from photovoltaic solar cells," *SoEn,* vol. 159, pp. 318-328, 2018/01/01/ 2018, doi: https://doi.org/10.1016/j.solener.2017.10.078.

[66] T. W. Teo, Z. Mahdavipour, and M. Z. Abdullah, "Recent advancements in micro-crack inspection of crystalline silicon wafers and solar cells," *MeScT,* vol. 31, no. 8, p. 081001, 2020, doi: 10.1088/1361-6501/ab8088.

[67] J. Carstensen, G. Popkirov, J. Bahr, and H. Föll, "CELLO: an advanced LBIC measurement technique for solar cell local characterization," *Sol. Energy Mater. Sol. Cells,* vol. 76, no. 4, pp. 599-611, 2003/04/01/ 2003, doi: https://doi.org/10.1016/S0927-0248(02)00270-2.

[68] O. Breitenstein *et al.,* "Can Luminescence Imaging Replace Lock-in Thermography on Solar Cells?," *IEEE Journal of Photovoltaics,* vol. 1, no. 2, pp. 159-167, 2011, doi: 10.1109/JPHOTOV.2011.2169394.

[69] T. Trupke, R. A. Bardos, M. C. Schubert, and W. Warta, "Photoluminescence imaging of silicon wafers," *Appl. Phys. Lett.*, vol. 89, no. 4, p. 044107, 2006, doi: 10.1063/1.2234747.

[70] P.-Y. Chen, M.-H. Tsai, W.-K. Yeh, M.-H. Jing, and Y. Chang, "Relationship between wafer edge design and its ultimate mechanical strength," *MiEng*, vol. 87, no. 11, pp. 2065-2070, 2010/11/01/ 2010, doi: https://doi.org/10.1016/j.mee.2009.12.083.

[71] C. L. Muhlstein, S. B. Brown, and R. O. Ritchie, "High-cycle fatigue and durability of polycrystalline silicon thin films in ambient air," *Sensors and Actuators A: Physical*, vol. 94, no. 3, pp. 177-188, 2001/11/20/ 2001, doi: https://doi.org/10.1016/S0924-4247(01)00709-9.

[72] W. W. V. Arsdell and S. B. Brown, "Subcritical crack growth in silicon MEMS," *JMemS*, vol. 8, no. 3, pp. 319-327, 1999, doi: 10.1109/84.788636.

[73] A. Danilewsky *et al.*, "Crack propagation and fracture in silicon wafers under thermal stress," (in eng), *J. Appl. Crystallogr.*, vol. 46, no. Pt 4, pp. 849-855, 2013, doi: 10.1107/S0021889813003695.

[74] J. G. E. Gardeniers, H. A. C. Tilmans, and C. C. G. Visser, "LPCVD silicon-rich silicon nitride films for applications in micromechanics, studied with statistical experimental design*," *Journal of Vacuum Science & Technology A: Vacuum, Surfaces, and Films*, vol. 14, no. 5, pp. 2879-2892, 1996, doi: 10.1116/1.580239.

[75] A. G. Noskov, E. B. Gorokhov, G. A. Sokolova, E. M. Trukhanov, and S. I. Stenin, "Correlation between stress and structure in chemically vapour deposited silicon nitride films," *Thin Solid Films*, vol. 162, pp. 129-143, 1988/08/01/ 1988, doi: https://doi.org/10.1016/0040-6090(88)90201-5.

[76] H.-I. Lee *et al.*, "Degradation by water vapor of hydrogenated amorphous silicon oxynitride films grown at low temperature," (in eng), *Sci. Rep.*, vol. 7, no. 1, pp. 14146-14146, 2017, doi: 10.1038/s41598-017-14291-2.

[77] G. I. N. Waterhouse, G. A. Bowmaker, and J. B. Metson, "Oxygen chemisorption on an electrolytic silver catalyst: a combined TPD and Raman spectroscopic study," *ApSS*, vol. 214, no. 1, pp. 36-51, 2003/05/31/ 2003, doi: https://doi.org/10.1016/S0169-4332(03)00350-7.

[78] X. Bao *et al.*, "The effect of water on the formation of strongly bound oxygen on silver surfaces," *CatL*, vol. 32, no. 1-2, pp. 171-183, 1995, doi: 10.1007/bf00806112.

[79] X. Bao, M. Muhler, T. Schedel-Niedrig, and R. Schlögl, "Interaction of oxygen with silver at high temperature and atmospheric pressure: A spectroscopic and structural analysis of a strongly bound surface species," *PhRvB*, vol. 54, no. 3, pp. 2249-2262, 07/15/ 1996, doi: 10.1103/PhysRevB.54.2249.

[80] R. Wiesinger, I. Martina, C. Kleber, and M. Schreiner, "Influence of relative humidity and ozone on atmospheric silver corrosion," *Corros. Sci.*, vol. 77, pp. 69-76, 2013, doi: 10.1016/j.corsci.2013.07.028.

[81] G. Gouadec and P. Colomban, "Raman Spectroscopy of nanomaterials: How spectra relate to disorder, particle size and mechanical properties," *Prog. Cryst. Growth Charact. Mater.*, vol. 53, no. 1, pp. 1-56, 2007/03/01/ 2007, doi: https://doi.org/10.1016/j.pcrysgrow.2007.01.001.

[82] Y. Han, R. Lupitskyy, T.-M. Chou, C. M. Stafford, H. Du, and S. Sukhishvili, "Effect of Oxidation on Surface-Enhanced Raman Scattering Activity of Silver Nanoparticles: A

Quantitative Correlation," *Anal. Chem.,* vol. 83, no. 15, pp. 5873-5880, 2011/08/01 2011, doi: 10.1021/ac2005839.

[83] A. G. Martin and M. J. Keevers, "Optical properties of intrinsic silicon at 300 K," *Progress in Photovoltaics: Research and Applications,* vol. 3, 1995.